The Thesis Committee for Sai Pranav Uppati
certifies that this is the approved version of the following thesis:

Investigation of Pulse Fracturing via Peridynamics Modeling and Simulation

APPROVED BY

SUPERVISING COMMITTEE:

John T. Foster, Supervisor

Kamy Sepehrnoori

Investigation of Pulse Fracturing via Peridynamics Modeling and Simulation

by

Sai Pranav Uppati, B.S.Ch.E.

THESIS

Presented to the Faculty of the Graduate School of

The University of Texas at Austin

in Partial Fulfillment

of the Requirements

for the Degree of

Master of Science in Engineering

THE UNIVERSITY OF TEXAS AT AUSTIN

December 2016

This thesis is dedicated to my loving parents and sister, who have guided me throughout my life both academically and personally. My successful completion of this degree and my positive outlook on the future are a testament to their unconditional love, and support.

Acknowledgments

I would first like to thank my thesis advisor, Dr. John T. Foster. First, the door to his office was always open to discuss anything I had on my mind, from research guidance to career advice. He always took the time to help me in any way that I needed. Second, when I was learning how to conduct computational research, he allowed me ample freedom to find my own way of learning. I believe his advising style is well suited for a research environment, where freedom and flexibility make way for creative thinking and problem solving. Third, he cared about my professional goals and was always supportive of my choices. He was also instrumental in getting my career started in industry. I am forever grateful to him for that. Finally, in the challenging field of peridynamics, his advice to keep pushing forward and tackle obstacles as they come helped me overcome some very difficult tasks. I've come to realize that this philosophy applies in life situations as well, and I will always remember to heed his advice.

I would also like to thank the sponsor of this research project, Andrew Gorton, who is a technical manager at the GE Global Research Center in Oklahoma City. Without interest from his team and GE's financial support, I would not have had the opportunity to work on such a challenging research area and learn some valuable coding skills as well as relevant oil and gas knowledge.

I completed a majority of the simulation work for this project during my summer internship at GE. Andrew, who was also my manager during the internship, helped provide context and ideas for me to make relevant progress in this research.

I would also like to acknowledge Michael Brothers and Jason York, fellow graduate students and researchers under Dr. Foster, who have helped me many times with computational modeling and peridynamics related questions. I also want to thank Moien Farmahini, who was a major help in my research during the internship.

Dr. Kamy Sepehrnoori, who was the second reader for my thesis, was also very helpful and prompt. I am grateful to him for his valuable comments on this thesis.

Finally, I must express my gratitude to my parents and to my friends for providing me with continuous encouragement throughout my graduate education and through the process of researching and writing this thesis. Thank you.

Investigation of Pulse Fracturing via Peridynamics Modeling and Simulation

Sai Pranav Uppati, M.S.E.
The University of Texas at Austin, 2016

Supervisor: John T. Foster

Pulse fracturing is an alternative stimulation technology to enhance production from oil and gas wells, especially ones in fractured hydrocarbon reservoirs. This stimulation generates multiple radial fractures that initiate at the wellbore wall, via the application of pressure pulses at rates on the order of 10 $\mathrm{MPa\,ms^{-1}}$ or more. These radial fractures act as conductive pathways for hydrocarbon flow into bottom of the wellbore. Pulse fracturing has been tested via experiments and oil field implementations quite extensively in the 1970s and 1980s.

The fracture mechanics of pulse stimulation, however, is not well understood. Computational efforts at modeling pulse fractures are relatively sparse in literature. Due to a recent renewal of interest in this form of stimulation, this computational study aims to develop a tool to simulate pulse fracturing. At the high loading rates experienced by rock during pulse stimulation, dynamic fracturing is expected to occur leading to the

generation of a complex radial fracture network. A state-of-the-art continuum mechanics code called *Peridigm* is well equipped to handle dynamic fracture modeling. *Peridigm*'s capabilities are explored to ascertain whether it can capture pulse fracture behavior accurately.

Using concrete as the computational medium, the relevant modeling considerations are analyzed to determine the best approaches for modeling pulse fracturing in *Peridigm*. This tailored approach is then used for benchmarking *Peridigm* against published pulse fracturing experiments on sandstone core samples.

Table of Contents

List of Tables

List of Figures

Chapter 1

Introduction

1.1 Hydrocarbons and fractured systems

Owing largely to emerging economies such as India and China, global GDP is expected to more than double by the year 2035 (British Petroleum Energy Report, 2016). This growth in global output, along with improvements in energy efficiency, predicts a rise in energy demand of 34% over the same timeframe. In the base case laid out in British Petroleum's 2016 Energy Outlook, fossil fuels will supply 80% of the energy demand in 2035. While demand for coal is expected to slow due to economic reform in China, oil and gas are expected to remain crucial energy sources. Specifically, natural gas is the fastest growing energy source in the fuel mix, due to the steady increase of US shale gas and liquified natural gas (LNG) supplies as well as supportive environmental policies. Oil, on the other hand, is expected to hold a steady growth rate, although the percent share of energy consumption powered by oil will likely decrease. The relevant sources of energy and their respective shares in energy demand are shown in Fig. 1.1. It is evident from the figure that oil and gas resources are going to be highly relevant for at least the next two decades.

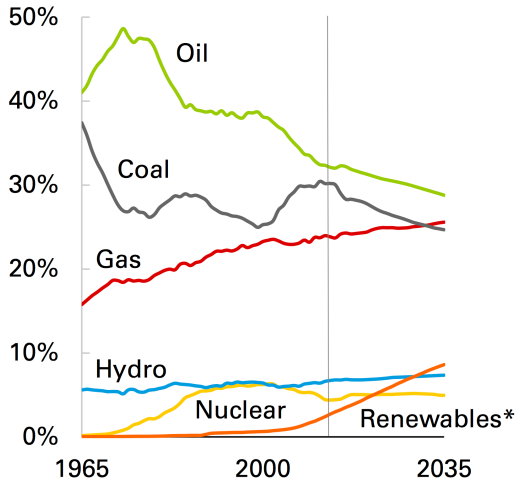

Figure 1.1: Shares of primary energy sources, 1965-2035. (British Petroleum Energy Report, 2016)

Hydrocarbon reserves are found in sedimentary basins around the world. Among these reserves, a significant portion are found in fractured systems. According to a 2008 Schlumberger report, "more than 60 percent of the world's proven oil reserves and 40 percent of the world's gas reserves" are trapped in fractured carbonate reservoirs (Schlumberger Brochure, 2008). To a lesser extent, even some of the world's organic-rich shale systems exhibit natural fractures. For instance, the Barnett shale of the Fort Worth basin in Texas consists of a system of natural fractures (Gale et al., 2007). While hydrocarbon recoveries from shales and carbonates are typically lower than from sandstone formations, this very same challenge makes these hydrocarbon sources high potential targets for increasing production (Schlumberger Brochure, 2008). Given that high demand for oil and gas energy will continue for decades to come, the importance of effectively

producing hydrocarbons from these fractured systems cannot be overstated. Naturally fractured reservoirs, therefore, stand to play an increasingly critical role in the future.

1.2 Stimulation and production enhancement

In order to meet the projected energy demand, it is more realistic to sustain and potentially improve production from existing oil and gas fields than to rely on making new oilfield discoveries (Schlumberger Brochure, 2008). Based on this mindset, currently producing oil and gas wells in fractured reservoirs should be prime targets for production enhancement. Therefore, a discussion of certain stimulation technologies, whose purpose it is to improve flow conductivity and counteract production declines, is highly appropriate.

Since the dawn of the unconventionals, stimulation, in the form of hydraulic fracturing, has been an integral part of the hydrocarbon extraction process. Stimulation is especially important for naturally fractured carbonate and shale systems because of the presence of a low permeability matrix. Hydraulic fracturing is not necessarily the best form of stimulation for fractured reservoirs. If the natural fracture system is primarily influenced by the in-situ stresses, it is unlikely that hydraulic fractures intersect these natural fractures (Stoller et al., 1985). In this case, hydraulic fractures propagate parallel to natural fractures, and hence do not connect the natural fracture system to the wellbore (Cuderman et al., 1986a). This type of

connectivity is important when the fluid flow is fracture dominated rather than matrix dominated.

1.3 Research motivation

Clearly, there is a need to find a reliable approach to sustain production levels in the world's fractured hydrocarbon reservoirs. As a potentially more effective alternative compared to hydraulic fracturing, high energy gas fracturing (HEGF), also known as pulse fracturing, is a candidate stimulation technology that was heavily researched, by way of experiments and field testing, in the 1970s and 1980s. Today, pulse fracturing is gaining renewed interest among academics and industry alike. According to Cuderman et al., 1986, it is a pertinent solution to fracture dominated flow in naturally fractured reservoirs (Cuderman et al., 1986a).

Pulse fracturing describes a stimulation process using a pressure source, such as a propellant, that provides a much higher rate of pressure loading than hydraulic fracturing, causing multiple radial fractures to initiate and propagate from the wellbore. For this reason, pulse fracturing is also sometimes referred to as multiple fracturing. If multiple fractures propagate to significant lengths, then the intersection between the created and natural fractures becomes extremely beneficial to production. This work focuses on studying pulse fracturing and its efficacy in enhancing production using computational modeling and simulation tools.

1.4 Research objectives

The primary goal of this work is to determine whether pulse fracturing is an effective stimulation technology, or at least elucidate the resulting fracture behavior under various subsurface conditions. The most cost effective way to achieve this goal is to use a calibrated predictive modeling tool to make decisions. Peridynamic simulation tools may well be appropriate for studying pulse fracturing. Arguably the best peridynamics code available to date, *Peridigm* is the simulation tool used for this research (Littlewood, 2015). Two main objectives are pursued in this study on pulse fracture modeling:

1. Assess the capability of *Peridigm* simulations to capture the multiple radial fracture generation from pulse loading, and investigate the requisite modeling choices that tailor *Peridigm* for pulse fracture modeling.

2. Benchmark *Peridigm* by comparison of simulation results with Lawrence-Livermore pulse fracture experiments on sandstone core samples.

1.5 Outline

This thesis contains four additional chapters following this one. Chapter 2 provides a literature survey of pulse fracturing and peridynamic theory. First, pulse fracturing is explained and some key experiments and field implementations are analyzed to understand the relevance of pulse

stimulation in the oil and gas industry. Subsequently, a motivation for computational modeling of pulse fracturing is developed. The peridynamic approach to fracture modeling is presented along with a brief introduction to the theory of peridynamics. Chapter 3 presents the modeling considerations relevant in the realm of peridynamic simulations and how they may be applied to pulse fracturing. It also describes the plan for this computational study. Chapter 4 explains the results from all the simulations, the modeling knowledge gained from the assessment stage of simulations, and the comparison between pulse fracture experiments and *Peridigm* simulation results. Chapter 5 summarizes the relevant observations and provides recommendations for developing *Peridigm* further as well as continuing the computational study on pulse fracturing.

Chapter 2

Background

This chapter provides a literature survey of pulse fracturing and peridynamic theory. Intially, pulse fracturing is defined and its advantages explained. A few key experimental studies and field implementations are presented to demonstrate the efficacy of pulse stimulation. Prior computational efforts to model pulse fracturing are also presented. Subsequently, the peridynamic approach to modeling pulse fracturing is suggested. A brief background on the peridynamic theory then follows, finishing up with an introduction to the computational code *Peridigm*.

2.1 Pulse fracturing

A candidate stimulation technology that was heavily researched in the 1970s and 1980s, pulse fracturing is a pertinent solution to such fracture dominated flow in naturally fractured reservoirs (Cuderman et al., 1986a). Pulse fracturing describes a stimulation process using a pressure source such as a propellant that provides a much higher loading rate of pressure than hydraulic fracturing, allowing multiple radial fractures to initiate and propagate from the wellbore. For this reason, pulse fracturing is also

sometimes referred to as multiple fracturing. If multiple fractures propagate to significant lengths, then the intersection between created and natural fractures becomes beneficial to production. This review paper will look at initial pulse fracturing experiments, some field cases studied and the present status of this technology, as well as provide suggestions for future work to exploit its potential.

Pulse fracturing was under rapid development in the former Soviet Union in the 1970s (Li et al., 1995). It started gaining interest among researchers in the United States in the late '70s. In the late '70s and early '80s, some of the first pulse fracturing experiments under realistic in-situ overburden and far-field lateral stresses were conducted by Sandia National Laboratories in the Department of Energy's Nevada Test Site (NTS). A discussion of pulse fracturing generally begins with comparison of this technology with other stimulation approaches, such as hydraulic fracturing and explosive fracturing (Warpinski et al., 1978).

2.1.1 Types of fracturing

There are three main fracturing regimes (Cuderman et al., 1986a). They are, namely, explosive fracturing, hydraulic fracturing, and multiple fracturing or pulse fracturing. Each regime is characterized by certain key features. First, the explosive fracture regime involves detonating a high-order explosive that crushes rock around the wellbore. The rate of loading is extremely high ($>$ 1500 psi/µs or 10 000 MPa ms^{-1}) and so are the peak

pressures attained (Warpinski et al., 1978). While the intention may be to stimulate the rock and increase the near wellbore permeability, the resulting crushing and compaction of the rock may seal off any cracks produced such that there is actually wellbore damage induced and a net reduction in conductivity.

Second, the hydraulic fracture regime uses fluid to pressurize rock beyond the in-situ stress to initiate and propagate fractures. The rate of loading is relatively low ($<< 0.1\,\text{psi}/\mu\text{s}$ or $0.7\,\text{MPa}\,\text{ms}^{-1}$) and so are the peak pressures attained (Warpinski et al., 1978). The characteristic result is a bi-wing planar fracture that aligns with the in-situ stresses, and, many times, does little to connect the natural fracture system to the wellbore (Cuderman et al., 1986a; Warpinski et al., 1978).

Third, the pulse fracturing regime is characterized by intermediate loading rates, the range for which is not clearly defined and differs depending on the source. Most commonly, the loading rates considered to be in this fracturing regime lie between $\sim 1.5\,\text{psi}/\mu\text{s}$ ($10\,\text{MPa}\,\text{ms}^{-1}$) and $\sim 30\,\text{psi}/\mu\text{s}$ ($200\,\text{MPa}\,\text{ms}^{-1}$) (Cuderman et al., 1986a; Swift et al., 1980; Warpinski et al., 1978). The peak pressures are typically $\sim 1 \times 10^4\,\text{psi}$ ($10 - 100\,\text{MPa}$) (Swift et al., 1980; Warpinski et al., 1978). The pressure loading is done through the use of propellants instead of high-explosives (Cuderman et al., 1986b). These propellants deflagrate or burn rather than detonate. The rate of pressure loading is controlled by appropriately selecting the grain sizes and burning characteristics of the solid propellants used. Controlled loading produces

multiple radial fractures that propagate from the wellbore, given that pressure is maintained by the continued burning of the propellant (Warpinski et al., 1978). The typical multiple fracturing pattern is shown in Fig 2.1. Given that significant lengths of these multiple fractures are attained, they can intersect the natural fracture system and connect it to the wellbore.

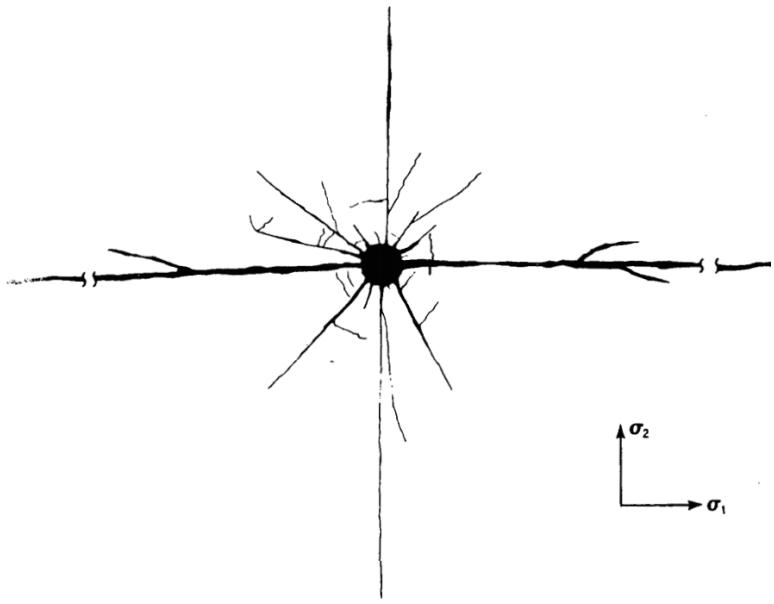

Figure 2.1: Typical fracture pattern observed at intermediate loading rates. (Cuderman et al., 1986a)

To understand when these regimes are observed, it is simpler to look at uncased boreholes, as casing adds additional variables to the mix. In uncased boreholes, the primary quantity that governs which regime a certain stimulation process falls into is the pressure risetime (Cuderman et al., 1986a). The pressure risetime, a function of borehole diameter and rock

type, defines the duration it takes to build pressure from the initial value to the peak pressure observed for the given fracturing process. For the stimulation to be in the pulse fracturing regime, the risetime t_m should fall in the following range (Cuderman et al., 1986a):

$$\frac{\pi D}{2C_R} < t_m < \frac{8\pi D}{C_R}, \tag{2.1}$$

where, D refers to the borehole diameter and C_R denotes the Rayleigh surface wave velocity, which is a material property specific to each rock type (Cuderman et al., 1986a).

Values of t_m at or below the lower limit refer to risetimes that are extremely short, which suggest high-explosives and the explosive fracture regime. On the other hand, values of t_m at or above the upper limit refer to risetimes that are relatively long, which indicate lower pressure loading rates and the hydraulic fracture regime. Risetimes and corresponding fracture regimes in relation to varying borehole size are depicted in Fig. 2.2. The specific rock used to obtain data for this plot was ash fall tuff.

From the plot, it is evident that the size of the t_m range for the pulse fracturing regime increases with borehole diameter. The magnitudes of the upper and lower bounds themselves also increase with borehole diameter. This phenomenon suggests that for larger boreholes, a slower-burning propellant is needed to achieve an equivalent fracturing regime (Cuderman et al., 1986a). Additionally, given the rock's specific C_R value and the borehole diameter D, a

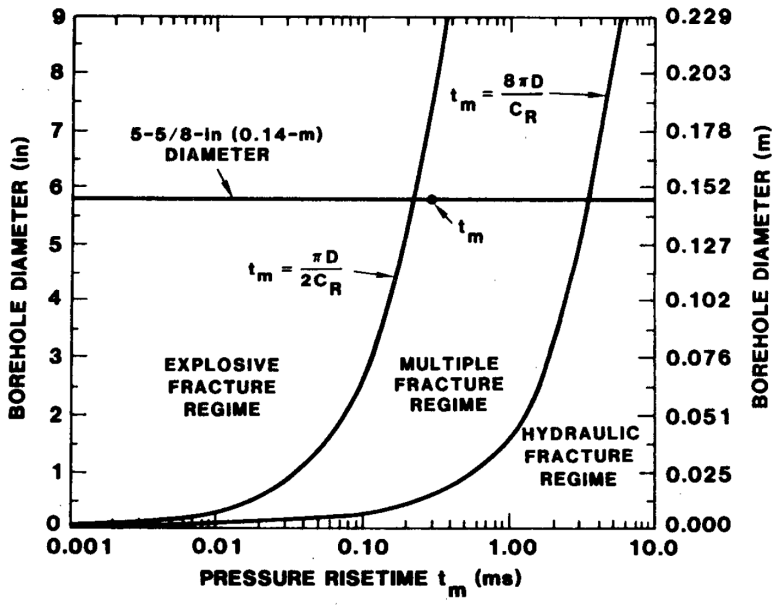

Figure 2.2: Fracture regime division based on pressure risetimes of ash fall tuff. (Cuderman et al., 1986a)

risetime range can be specified to produce multiple fracturing. Propellants that satisfy the required pressure risetime range may then be appropriately used. In order to better understand the fracturing behavior during pulse loading, it's necessary to look at the experiments conducted by Sandia under realistic in-situ conditions.

2.1.2 Experimental observations: uncased boreholes

In the late 1970s, the first pulse fracturing experiments were conducted under realistic in-situ stresses in the G-tunnel complex at the Nevada Test Site (NTS). Laboratory experiments and small-scale tests for multiple fracturing had been performed before, but had never incorporated realistic stresses. The

rock type in these experiments was ash fall tuff. The overburden at this location was approximately 1400 ft, which amounts to an overburden pressure of ∼1000 psi (Warpinski et al., 1978). Three pilot holes of 8 in diameter each were used with three different propellants, each with a characteristic burn rate. The experiments were conducted in uncased boreholes. The experimental setup is schematically shown in Fig. 2.3. In this setup, GF1 represents gas frac experiment 1 with the slow propellant. GF2 is associated with the intermediate propellant. And, GF3 is associated with the fast propellant. The results were analyzed using the pressure-time records and direct viewing of the fractures. The fractures were observed by posttest mineback.

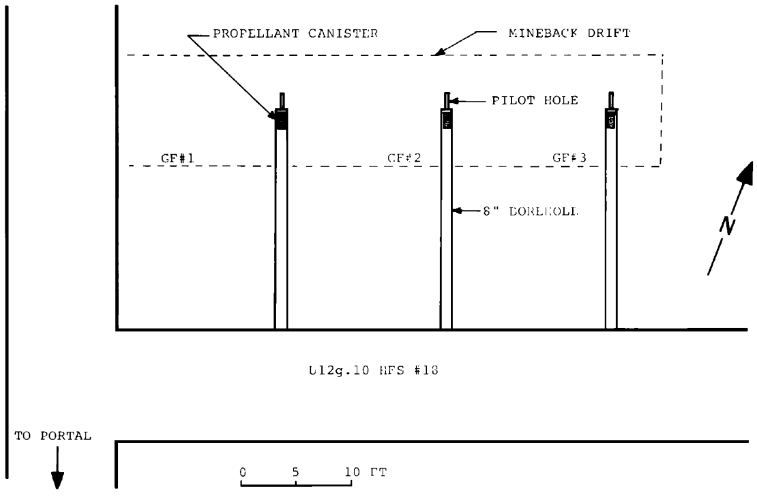

Figure 2.3: First high energy gas frac experiemental setup under realistic stresses. (Warpinski et al., 1978)

The record from GF1 showed a pressure loading rate of ∼0.09 psi/µs with a peak at 6250 psi (Warpinski et al., 1978). The mineback revealed an

approximately 3 ft long fracture to the southwest that also extended ∼2 ft to the northeast. This direction is normal to the minimum principle in-situ stress, which suggests that GF1 essentially represents a small hydraulic-type fracture. Meanwhile, the GF2 record showed a loading rate of ∼20 psi/µs with a peak at 13 800 psi. The pressure-time record is depicted in Fig. 2.4.

As shown in the plot, pressure spikes to an initial peak, then decreases, before rising to a second peak. The first peak is reached when the fractures initiate (Warpinski et al., 1978). The decrease in pressure is associated with sudden increase in free volume following fracture initiation (Cuderman et al., 1986c). Fracture growth after initiation takes place at a lowered rate in terms of opening up additional volume, which allows pressure to build again (Cuderman et al., 1986c). This type of loading produced 12 different fractures, 5 of which were small (< 1 ft) and the remaining relatively long ($2 - 8$ ft) (Warpinski et al., 1978). The orientations of the fractures include some that were at large angles with the borehole, while other were relatively parallel to it. A computer facsimile of the top view, shown in Fig. 2.5, illustrates various fracture planes of the initiated fractures, modeled after the original mineback.

Finally, the pressure-time record from GF3 indicated a loading rate greater than 1500 psi/µs, with a peak greater than 30 000 psi (Warpinski et al., 1978). Mineback from this experiment revealed one significant fracture (∼4 ft) radially from the wellbore, numerous small incipient fractures, and a crumbled zone (∼$2-4$ in thick) around the wellbore, which are characteristic of explosive

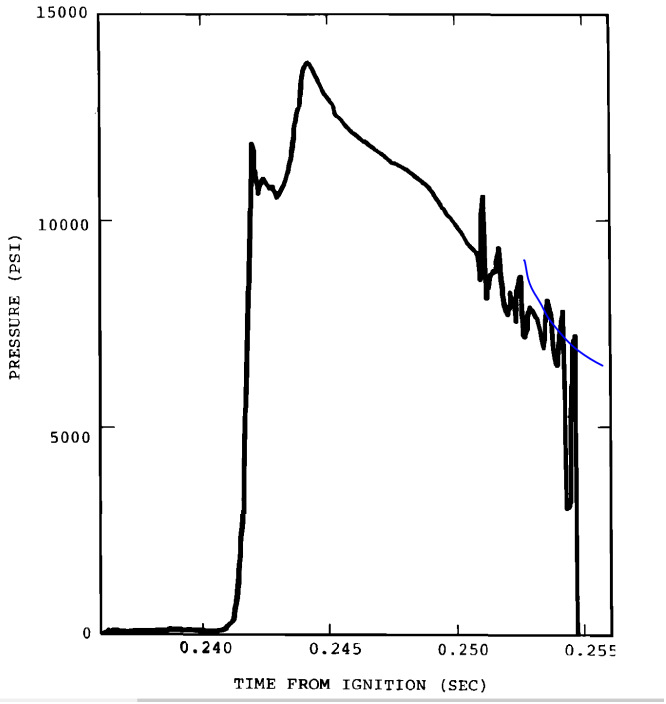

Figure 2.4: Pressure-time record for gas frac experiment 2 (GF2), showing the characteristic loading profile for multiple fracturing. (Warpinski et al., 1978)

fracturing. In these experiements, GF2 represents the desirable behavior of multiple fracturing. While Warpinski et al. admit that "realistic calculations for...final crack lengths will require knowledge of the gas dynamics and the actual pressure loading in the cracks", the analytically-derived upper limit for the multple fracture length in this specific experiment was 30 ft, which is encouraging (Warpinski et al., 1978).

Warpinski et al. state that this realistic experiment demonstrates that multiple fracturing is possible under in-situ stresses, given that the tailored propellant provides "(1) a high enough loading rate to initiate multiple

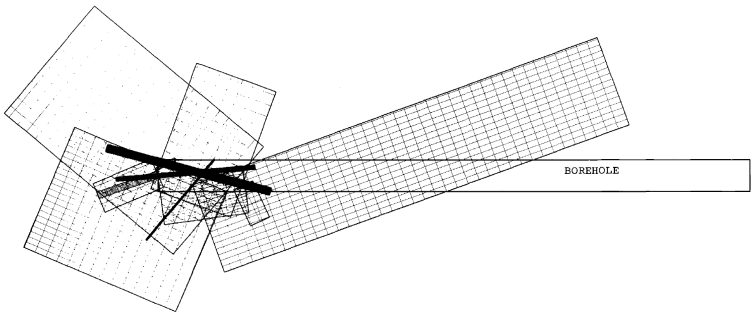

Figure 2.5: A computer facsimile of the fracture planes observed in GF2, indicating multiple fracture orientations. (Warpinski et al., 1978)

fractures, (2) high enough pressures to extend fractures radially, but not so high as to exceed the flow stress of the rock, and (3) sufficient gas generation to allow most of the fractures to be pressurized and propagated further" (Warpinski et al., 1978). They admit that the fractures didn't grow long enough to understand the effects of in-situ stresses on fracture orientaion. These results, while they support the potential of pulse fracturing to establish connectivity between wellbores and natural fractures, were only preliminary.

2.1.3 Experimental observations: cased boreholes

For uncased boreholes, it has been shown that pressure risetime t_m, which reflects the rate of loading, is the primary factor that determines fracture behavior. To understand multiple fracture behavior in cased boreholes, Cuderman conducted the first detailed tailored-pulse fracturing study in cased and perforated boreholes under realistic in-situ stresses (Cuderman et al., 1986b). These experiements were also conducted in the

G-tunnel complex at the Nevada Test Site (NTS). The overburden used here was 1000 psi. As in the uncased experiments, the fractures were directly observed via posttest mineback. While the primary objective remained determining whether multiple fracturing can be obtained through perforations, they also paid close attention to resultant casing damage.

Cuderman conducted eight experiments, labeled A-H, at NTS. Fig. 2.6 lists values of parameters chosen in each experiment. As shown in the table, parameters that were varied include borehole depth, presence or absence of fluid, perforation density, perforation diameter, perforation phasing, propellant type, amount of propellant and canister size. Experiments E, F and G have higher perforation density and diameter than the others. Phasing refers to the separation in degrees between perforations within the same set. For instance, a phasing of 120° means that at one lateral position on the cylindrical casing, three perforations are made equally spaced apart in a circle. Similarly, 90° indicate 4 perfs and 180° indicate 2 perfs.

The fracture patterns and casing damage, if any, with these eight experiments are shown in Fig. 2.7, where σ_3 represents the minimum principal stress. Among the set of experimental results, the ones from A, B, E and G provide key insights (Cuderman et al., 1986b). A and B were designed such that gas doesn't exit via the perforations during propellant deflagration. The parameters were mostly the same for A and B, except for small differences in the propellant grain size and the amount of propellant

			Perforations			Propellant		
Experiment	Borehole Depth (m [ft])	Wet/ Dry	Perfs per meter (ft)	Perf Diameter (mm [in])	Phasing (deg)	Type	Weight (kg [lb])	Canister O.D. (m [in])
A	12.2 (40)	Dry	13 (4)	9.5 (0.375)	120	M5(B)	2.15 (4.75)	0.044 (1.75)
B	12.2 (40)	Dry	13 (4)	9.5 (0.375)	120	M5(A)	1.81 (4.00)	0.044 (1.75)
C	7.6 (25)	Dry	13 (4)	9.5 (0.375)	90	M5(B)	2.72 (6.00)	0.044 (1.75)
D	7.6 (25)	Wet	13 (4)	9.5 (0.375)	90	M5(B)	2.38 (5.25)	0.044 (1.75)
E	7.6 (25)	Wet	20 (6)	15 (0.6)	120	M30(B)	4.65 (10.25)	0.068 (2.66)
F	7.6 (25)	Wet	20 (6)	15 (0.6)	120	M5(B)	5.90 (13.00)	0.068 (2.66)
G	7.6 (25)	Dry	20 (6)	15 (0.6)	120	M30(B)	4.69 (10.35)	0.068 (2.66)
H	7.6 (25)	Wet	13 (4)	9.5 (0.375)	180	M5(A)	2.09 (4.60)	0.044 (1.75)

Figure 2.6: Experimental parameter list for eight experiments conducted with cased boreholes by Cuderman. (Cuderman et al., 1986b)

used. The same or similar pressure profile was expected for A and B. This pressure profile indicates a risetime of 2 ms and a peak pressure of 20 000 psi (Cuderman et al., 1986b). The mineback revealed that fractures initially grew in the direction that the perforations opened, but eventually turned toward the typical hydraulic fracture direction, as is evident from the fracture patterns of A and B. Fractures up to 8 ft were observed for these two experiments. A single split in casing was observed in each experiment, although casing was not compromised and remained intact in both.

Experiments E and G, on the contrary, were purposefully designed to allow maximum gas flow through perforations (Cuderman et al., 1986b). Between these two experiments, the only difference was that E included a water-filled borehole whereas G did not. The intention of these experiments was to limit the peak pressure attained and prevent or minimize casing damage. Using a large propellant grain size also facilitated longer burn times. The pressure profile for E shows a 6 ms risetime and a peak pressure

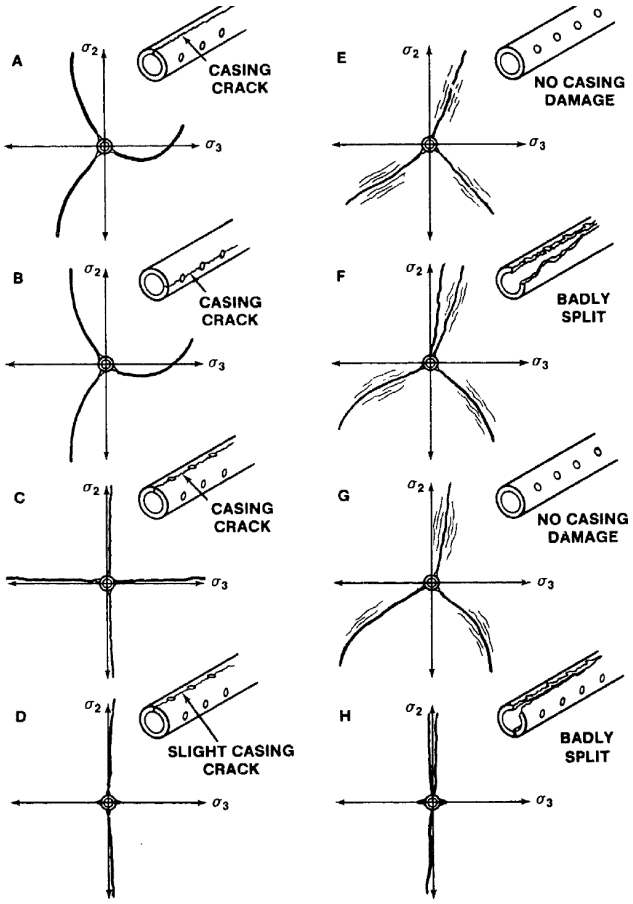

Figure 2.7: Fracture patterns observed and attendant casing damage (if any) for the 8 experiments. (Cuderman et al., 1986b)

of 12 600 psi (Cuderman et al., 1986b). On the other hand, G's profile indicates a risetime of 13.9 ms and a peak pressure of 16 500 psi (Cuderman et al., 1986b). The differences between E and G suggest that pressure risetimes are signficantly lower for liquid-filled boreholes compared to liquid-free boreholes, all other parameters equal. In addition, the peak pressures are considerably lower for liquid-filled boreholes. On the same note,

a slower-burning propellant is required to produce equivalent fracturing in a liquid-filled borehole relative to a liquid-free borehole (Cuderman et al., 1986a). Mineback showed that the fracturing behavior is similar to A and B in that as distance from wellbore increases, the orientation gradually turns normal to σ_3. Fractures extended beyond 10 ft (Cuderman et al., 1986b). No casing damage was observed in either case.

Experiments C, D, F and H provide additional data points. The primary takeaway from experiments A and B (and C as well) is that multiple fracturing can be attained even through perforations with little or no casing damage (Cuderman et al., 1986b). Meanwhile, the results from E and G suggest that, in liquid-filled or liquid-free boreholes, using the largest practical perforation size, high perforation density, and enough propellant amount to sustain long burn times, produces long multiple fractures with no attendant casing damage (Cuderman et al., 1986b). In fact, the propellant and perforation combination in E and G seems to be optimal. In experiment F, which was water-filled, a faster propellant relative to the one used in experiments E and G produced a higher loading rate and caused severe and permanent casing damage. The exceptions, experiments D and H (both water-filled), resulted only in hydraulic-type fractures, despite the perforation phasing. No sufficient explanation was given to explain this phenomenon.

2.1.4 Field observations

Pulse fracturing has shown promise in a controlled experimental setting in that it has the ability to produce multiple fractures that aren't initially guided by the far-field stresses. These radial fractures therefore can intercept the natural fractures, connecting them to the wellbore and enhancing production. However, without proper field testing, pulse fracturing's merits are all but speculative. The following field case studies shed more light on how pulse fracturing enhances oil well productivity.

2.1.4.1 Devonian shale, 1980s

After the initial Sandia experiments at NTS, one of the first real pulse fracturing field implementations took place in the mid 1980s. Pulse fracturing was applied to Devonian shale gas wells in Rowan County, KY and Meigs County, OH. Wells chosen in both locations were completed openhole and neither filled with fluid (Cuderman et al., 1986c). In these experiments, borehole tv logs were used to document the presence of natural fractures prior to using pulse stimulation and to observe fracturing attained post-stimulation (Cuderman et al., 1986c).

In Rowan County, two separate experiments were conducted. Experiment 1 was conducted at a depth that corresponded to the Lower Huron shale formation, with relatively low permeability. During the pulse fracturing procedure, the pressure record failed due to some issues, but post-stimulation production testing indicated an open flowrate of $1000\,\mathrm{ft}^3/\mathrm{d}$

where there was no prior measurable flow (Cuderman et al., 1986c). Experiment 2 was conducted at a depth that corresponded to the Middle Huron member of the Ohio shale. This formation was comparatively much less permeable. Pressure records were successfully obtained here, indicating a risetime of 0.9 ms and a peak pressure of 12 000 psi (Cuderman et al., 1986c). The borehole tv log revealed four fractures, which is consistent with multiple fracturing. The risetime was close enough to the multiple-hydraulic boundary that 4 fractures instead of 8 were produced in the treatment. Production, on the other hand, only amounted to about 35 ft^3/d, attributed to very tight lithology and lack of a significant number of natural fractures (Cuderman et al., 1986c).

In Meigs County, only one experiment was conducted. A specific well in the Lower Huron formation, with no prior stimulation done and a measurable pre-treatment production rate of 6700 ft^3/d, was chosen for pulse stimulation. A pressure pulse designed to produce a 0.33 ms risetime and eight fractures was implemented (Cuderman et al., 1986c). The pressure record indicates a risetime of 0.5 ms and a peak pressure of 16 000 psi, resulting in 4 fractures. The higher risetime is attributed to not incorporating into the design the free volume associated with natural fractures in the system (Cuderman et al., 1986c). The production, however, did gain a huge boost, with a post-stimulation flow rate of 22 000 ft^3/d (Cuderman et al., 1986c). The cause of enhanced production is difficult to place exactly, because nitrogen foam fracturing done on a nearby well

produced similar results. Cuderman et al. notes that it's possible that removing the near wellbore formation damage resulted in the production spike (Cuderman et al., 1986c). In this sense, pulse stimulation was successful, as skin factor decreased from +12 to -2 (Cuderman et al., 1986c).

From the experiments in Rowan and Meigs counties, multiple fracturing shows promise in enhancing gas recovery in shale formations. The difference in expected and measured pressure pulses suggests that free volume from natural fractures should be taken into account in the design. Doing so would allow appropriate propellant configurations to be chosen such that 8 fractures (or more), as designed, are produced instead of 4 (or less). These experiments also suggest that pulse stimulation is successful in intercepting the natural fractures and connecting them to the wellbore. Clearly, pulse fracturing is a technology worth exploring.

2.1.4.2 Thorold-Grimbsy sandstone, 1990s

In the 1990s, Telesis Oil and Gas company required clean up of wellbore damage in the Thorold-Grimbsy sandstone reservoir of Lake Erie. The stipulation was that the designed stimulation should not establish connectivity to the water zone below (Druet and O'Connor, 1991). Two wells were selected for stimulation, well 124-P-3 and well 124-F-2. Logs for both wells indicated that hydraulic fracture containment within the target zone was impossible (Druet and O'Connor, 1991). Computalog, the company that provided the pulse fracturing service, designed the program such that

perforations in casing had a density of 26 shots/m, as recommended by Cuderman's studies on tailored-pulse fracturing to minimize casing damage (Druet and O'Connor, 1991; Cuderman et al., 1986b). Pulse fracturing was then to be run twice over the interval designated for stimulation (Druet and O'Connor, 1991).

In well 124-P-3, tests prior to and post stimulation were done to accurately document any changes in well performance. Prior to stimulation, the well showed a permeability thickness kh of $305\,\mathrm{md-ft}$ (Druet and O'Connor, 1991). After the stimulation, kh increased to $435\,\mathrm{md-ft}$ (Druet and O'Connor, 1991), translating to an increase in permeability of 43%. The skin factor also decreased from +16.4 to +2.0 (Druet and O'Connor, 1991). Druet et al. state a quantity called deliverability, which apparently increased 4-fold due to pulse stimulation (Druet and O'Connor, 1991). These changes are attributed to pulse fracturing, which removes near wellbore damage by microfracturing the rock adjacent to the wellbore. It was commented that "[pulse fracturing] was successful at reducing skin damage, induced both by drilling operations and by cementing and completion operations", without compromising stimulation containment (Druet and O'Connor, 1991).

In well 124-F-2, similar pre- and post-stimulation testing were done. The results of the tests did not show as dramatic of an increase as in the previous well, but deliverability, as stated by Druet et al., increased by about 75% (Druet and O'Connor, 1991). Specifically, the permeability thickness kh increased from $44\,\mathrm{md-ft}$ to $79\,\mathrm{md-ft}$ due to pulse stimulation. Meanwhile,

the skin factor changed from -0.1 to -0.7.

Through both these field tests, it's evident that pulse fracturing is an option to be considered for decreasing skin and increasing the permeability. To clarify, skin is a dimensionless quantity representing an additional pressure drop caused by formation damage (PetroWiki Database, 2015). When skin is positive, the largest pressure drop possible between the formation and wellbore is not achieved, because the effective formation pressure is lower. The driving force of flow, the pressure drawdown, is less than 100%. Reducing skin factor is therefore important to enhancing hydrocarbon production. Pulse fracturing may thus be a good bet.

Among pulse fracturing field implementations, two cases, one in shale and the other in sandstone, were presented to demonstrate the strength and utility of pulse stimulation. The Devonian shale case, through production testing, has shown that pulse fracturing is successful at intercepting the natural fractures in a formation and potentially reducing near wellbore formation damage. The Thorold-Grimbsy sandstone case more quantitively illustrated the enhancement in near wellbore permeability and favorable skin by the use of pulse fracturing. While these resulting wellbore and near wellbore changes from pulse fracturing may enhance hydrocarbon production, they may also play a beneficial role in pre-hydraulic fracturing. By reducing the near wellbore formation damage, pulse fracturing minimizes any frictional pressure losses during hydraulic fracturing (Jaimes Plata et al., 2012). Pulse fracturing therefore is a multifaceted technology.

2.1.5 Challenges and motivation for computational modeling

The need for promoting pulse fracturing and its benefits is evident. Specifically, in relation to the recent shale boom in the United States, hydraulic fracturing may not always be the correct choice for shale stimulation. Within the past few years, Safari et al. pointed out that "[f]ield experience has shown that not all shale formations respond to hydraulic fracturing effectively" (Safari, 2013). They state that, with proper tailoring of the pulse fracture design, the transition from ductile to brittle behavior in shale can be triggered, which enables stimulation to produce "high quality, extensive and complex fracture networks that can remain open during production." Of course, pulse fracturing is by no means limited to application in shales. Yang et al. lists situations when pulse fracturing is highly appropriate (Yang et al., 1992):

1. Exploration wells, from which accurate log data is needed, can benefit from clean up via pulse stimulation.

2. Post-hydraulic fracturing stemming results in sub-par production, which can be eliminated by pulse fracturing.

3. Injection wells can benefit from pulse fracturing because it cleans up the plugged pores due to solid impurities in the water.

4. Pulse-induced fractures can intersect natural fissures and enhance production.

5. Formation layers with water sensitivity can benefit from pulse stimulation because its working fluid is gas.

Challenges do exist, however, with pulse fracturing. From the field cases analyzed, it was clear that the design predictions were not met during implementation. The fracture behavior from pulse stimulation is evidently more complicated than from hydraulic fracturing. Hence, *tailoring* the pulse fracture design, requires an understanding of the interplay between geomechanical propeties and fracture potential of formation rock and gas dynamics due to in-situ combustion (Safari et al., 2014). Modeling and simulation of pulse fracturing is the only cost-effective way to achieve this level of understanding.

Compared to experimental investigation of pulse fracturing, the amount of available literature discussing dynamic fracture modeling is considerably less. Safari et al. has published one of the more recent studies on modeling pulse stimulation (Safari et al., 2014). In this study, the ultimate fracture geometry achieved is attributed to two distinct types of loading: (1) dynamic loading from the propagation of stress waves, and (2) a much slower, quasistatic loading from the gas generated during in-situ propellant combustion. This idea suggests that the initial complex fracture pattern is generated by the dynamic loading. Subsequently, the quasistatic gas loading within the induced fracture network extends these fractures to significantly longer lengths. A combination of two softwares, Ansys AUTODYN and EFRAC3D, are used to study the dynamic and quasistatic

loading, respectively. Integrating the capabilities of both software, Safari et al. estimate that the dense fracture network generated can establish pathways from the wellbore ∼350 ft into the reservoir (Safari et al., 2014).

An alternative approach to modeling pulse fracturing is through modeling software based on the novel peridynamic theory. The theory of peridynamics is a generalization of the classical continuum mechanics theory to facilitate a unified treatment of fractures and continuous media in the same mathematical framework. The result is that fracture initiation and propagation naturally evolve in the process of numerically solving the integro-differential force balance equation of peridynamics. This theory has specifically been validated for dynamic brittle fracturing (Silling, 2014). A brief background on the peridynamic theory follows.

2.2 Brief background on peridynamics

2.2.1 General motivation for development of peridynamics

Peridynamics, also known as the peridynamic theory of solid mechanics, is an alternative formulation of continuum mechanics that lends itself well to handle the mathematical difficulties inherent in solving the equation of motion for discontinuous media. In continuum mechanics, the root of the problem is that, when there is a discontinuity in a medium e.g. a crack, the displacement field $\boldsymbol{u}(x, y, z)$ is discontinuous in space (Silling, 2000). Hence, any type of strain measure requires the first order spatial derivative of displacement $\boldsymbol{u}$, which becomes mathematically undefined along the discontinuity. Meanwhile,

higher orders derivatives of displacement are necessary to resolve the force balance in continuum mechanics. The equation of motion, a representation of Newton's second law, in differential form is shown below (Silling, 2014):

$$\rho \ddot{\boldsymbol{u}} = \nabla \cdot \overline{\overline{\sigma}} + \boldsymbol{b}, \tag{2.2}$$

where ρ is mass density, $\ddot{\boldsymbol{u}}$ is the kinematic acceleration defined as the second order time derivative of displacement, $\overline{\overline{\sigma}}$ is the stress tensor, and $\boldsymbol{b}$ is the body force density. The stress tensor $\overline{\overline{\sigma}}$ depends on the strain tensor $\overline{\overline{\epsilon}}$ in various ways, depending on the constitutive model used. Even for the simple case of pure linear elasticity, where the stress is a linear function of strain, the force balance in Eq. (2.2) requires evaluation of the second order spatial derivative of the discontinuous displacement field, owing to the divergence term on the right hand side of the equation.

To overcome this difficulty, methods of redefining the body where the discontinuity falls along the boundaries of the body have been extensively used (Silling, 2000). The disadvantage to using such a workaround is that it neccesitates knowledge of where the discontinuity is going to be located. Additionally, special techniques are needed to treat the discontinuities. The scope of compatible problems narrows considerably, given these restrictions. Especially when the initiation of fracture is of interest, a more comprehensive solution is necessary. Such is the motivation behind the development of peridynamic theory. Because the displacement field $\boldsymbol{u}(x, y, z)$ is spatially

discontinuous and spatial derivaties of it are undefined where fractures are present, peridynamic theory does away with classical measures such as strain and stress, which require partial differentiation with respect to space. In lieu of differentiation, integration is used in the evaluation of the force balance.

2.2.2 Bond-based peridynamic framework

The peridynamic analog of the classical equation of motion is an integro-differential equation, as given below (Silling et al., 2007):

$$\rho(\boldsymbol{x},t)\ddot{\boldsymbol{u}}(\boldsymbol{x},t) = \int_{\mathcal{H}_x} \boldsymbol{f}\left(\boldsymbol{u}\left(\boldsymbol{x}',t\right) - \boldsymbol{u}\left(\boldsymbol{x},t\right), \boldsymbol{x}' - \boldsymbol{x}\right) dV_{\boldsymbol{x}'} + \boldsymbol{b}(\boldsymbol{x},t), \qquad (2.3)$$

where the shift to a peridynamic framework is reflected in the integral term. The integral replaces the divergence term in the classical equation given by Eq. (2.2). The pairwise force function $\boldsymbol{f}$ embodies the constitutive relation for the material at hand. The integrand, a function of an arbitrary material point $\boldsymbol{x}$, is integrated over all $\boldsymbol{x}' \in \mathcal{H}_x$, where $\mathcal{H}_x$ is the called the *family* of $\boldsymbol{x}$. The internal forces in a given body are handled through this integral term.

In a given body $\mathcal{R}$, consider an arbitrary material point $\boldsymbol{x}$. $\mathcal{H}_x$ demarcates the spherical neighborhood around $\boldsymbol{x}$, with radius given by a quantity δ called the *horizon*. The horizon is typically considered a material property. In this peridynamic framework, the constitutive interaction, e.g. elastic, viscoelastic, and plastic, between $\boldsymbol{x}$ and $\boldsymbol{x}'$, as determined by $\boldsymbol{f}$, acts on the *bond* between the two points. The bond is mathematically

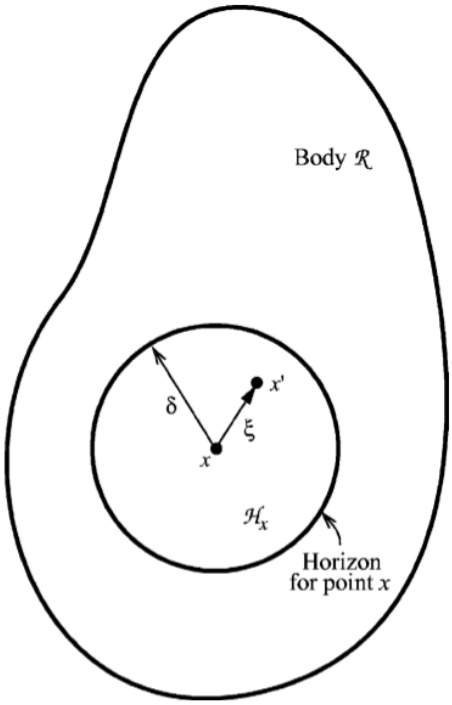

Figure 2.8: In a body $\mathcal{R}$ with a horizon δ, an arbitrary material point $\boldsymbol{x}$ with its respective family $\mathcal{H}_x$. (Silling and Askari, 2005)

represented, in the *reference* or undeformed configuration, by their relative position and is denoted $\boldsymbol{\xi} = \boldsymbol{x}' - \boldsymbol{x}$. These peridynamic quantities are illustrated in Fig. 2.8. The displacements of $\boldsymbol{x}$ and $\boldsymbol{x}'$, going from the reference configuration to the *current* or deformed configuration, are respectively denoted $\boldsymbol{u}$ and $\boldsymbol{u}'$. Their relative displacement is denoted $\boldsymbol{\eta} = \boldsymbol{u}' - \boldsymbol{u}$. Based on these definitions, it is clear that the current relative position, meaning post deformation, is given by $\boldsymbol{\eta} + \boldsymbol{\xi}$. Accoring to Eq. (2.3), $\boldsymbol{f}$ depends on $\boldsymbol{\eta}$ and $\boldsymbol{\xi}$. The significance of $\mathcal{H}_x$ is that (Silling et al., 2007),

$$|\boldsymbol{\xi}| > \delta \implies \boldsymbol{f}(\boldsymbol{\eta}, \boldsymbol{\xi}) = \mathbf{0} \quad \forall \boldsymbol{\eta}, \tag{2.4}$$

by which the implication is that the bonds of $\boldsymbol{x}$ outside $\mathcal{H}_x$ hold no force. The constitutive model only applies to the bonds within $\mathcal{H}_x$, affecting the material behavior at $\boldsymbol{x}$.

Given the basic structure of peridynamics, clear distinctions can be made between the classical and peridynamic approaches. Due to the direct interactions with material points other than the nearest neighbors, the peridynamic approach is categorized as *non-local*. This core feature is in stark contrast with the classical approach, in which strain is dependent only on contact forces, forces between material points that are in direct contact (Silling et al., 2007). Moreover, because the classical stress and strain measures are not used and Eq. (2.3) does not require spatial derivatives, the primary issue faced with the classical approach is no longer of concern.

2.2.3 Bond damage and fracture generation

Fractures are of primary interest in peridynamic modeling. Therefore, it is important to understand the origin of fracture in a peridynamic body. Bonds carry force in the peridynamic framework. When, according to some specified criterion, bonds irreversibly break, i.e. they no longer have the capacity to carry a force, their loads are shifted to neighboring bonds (Silling, 2014). This shifting may overload the neighboring bonds as well, causing them to fail. Eventually, this process leads to progressive failure of

bonds, resulting in a fracture. Such a process is illustrated in Fig. 2.9.

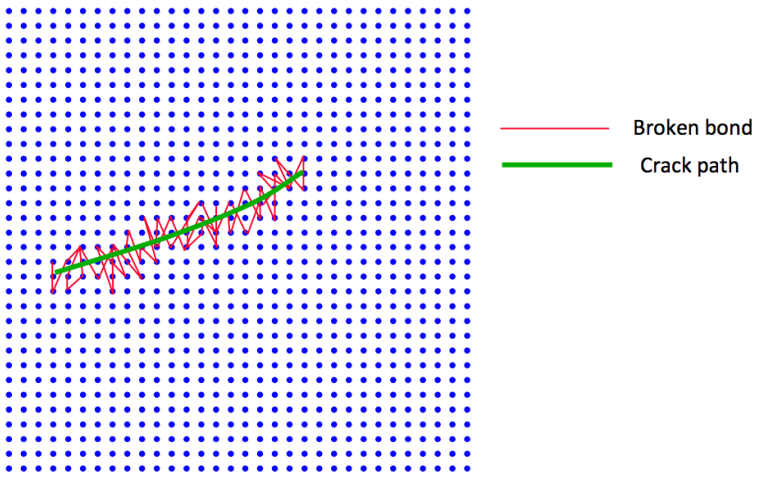

Figure 2.9: Progressive bond failure leads to a fracture. (Silling, 2014)

To understand bond damage criterion, for simplicity, consider an elastic material being modeled in a peridynamic framework. All the bonds of $\boldsymbol{\xi}$ within the family then carry force according to Hooke's law in 3D. This elastic material satisfies a linear relationship between the bond force density and the bond strain. A visual representation of the bond force and bond strain relation is given in Fig. 2.10. In this figure, the bond is damaged after some critical bond strain is achieved. This is known as the *critical stretch damage criterion*, which is the most common damage model used in peridynamic modeling.

Lastly, it is important to note the quantitative definition of damage. Damage is a quantity that is defined for each material point. It is defined as the ratio of the number of intact bonds in the current configuration to the

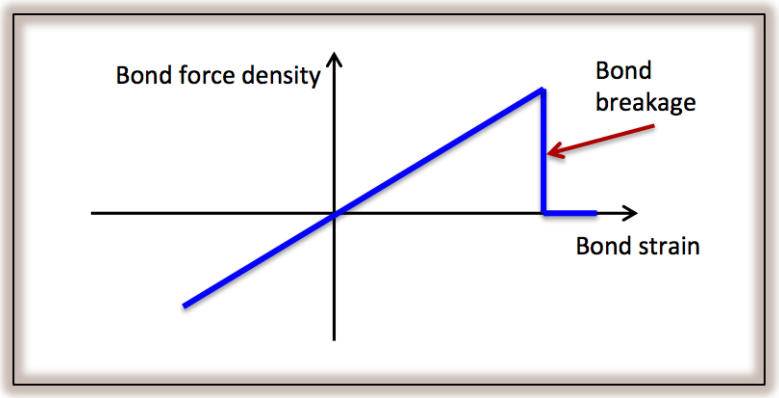

Figure 2.10: Bond force-strain relation in an elastic peridynamic body. (Silling, 2014)

number of original bonds in the reference configuration. It may be expressed as a fraction or percentage. A damage value of 0 denotes a material point that has not undergone any irreversible bond breakage. On the other hand, a damage value of 1 or 100% indicates a material point that no intact bonds left, meaning it has completely dislodged from the main body. Therefore, a plane which has points on either side with damage above 30-40% may be considered a fracture plane.

2.2.4 Numerical peridynamics

The peridynamic equation of motion is an integro-differential equation that has no analytical solution for most real scenarios. This theory is intended to solve complex fracture growth problems, which can only be done numerically. In the numerical framework of peridynamics, any domain is discretized into elements or nodes that have no geometrical connections to

each other (Silling and Askari, 2005). This setup is where the meshfree peridynamic method derives its name. Each element represents a certain volume of the domain. When combined together, the elements make up a grid, for which the spacing is denoted by Δx. Finally, the peridynamic equation of motion is also discretized, where a finite sum replaces the integral. It is given by (Silling and Askari, 2005)

$$\rho \ddot{\boldsymbol{u}}_i^n = \sum_p \boldsymbol{f}\left(\boldsymbol{u}_p^n - \boldsymbol{u}_i^n, \boldsymbol{x}_p - \boldsymbol{x}_i\right) V_p + \boldsymbol{b}_i^n, \tag{2.5}$$

where n denotes the time step number and the variable subscripts indicate the element number. V_p is the volume associated with element p.

The acceleration term, $\ddot{\boldsymbol{u}}_i^n$, is calculated based on a central difference formula, in which a constant time step size, Δt, is assumed. The truncation error for using finite difference approximations, in the case of fracture growth problems, is $O(\Delta x) + O(\Delta t^2)$. Moreover, for an explicit scheme, a stability criterion is a requirement. Depending on whether the material model is linear or nonlinear, the exact stability criterion varies. However, the general form of the stability criterion prescribes an upper bound for Δt. The setup described above comprises the essential numerical framework for peridynamic compuations.

2.2.5 Limitations of the bond-based theory

The peridynamic framework described so far, called the *bond-based* peridynamic theory, has been developed extensively in the early 2000s. However, the bond-based theory has some important limitations (Silling et al., 2007):

1. While all the bonds within $\mathcal{H}_x$ affect the force balance at $\boldsymbol{x}$, individual bonds $\boldsymbol{\xi} \in \mathcal{H}_x$ respond to loading independently of each other. This oversimplifies the material model and is not representative of most real materials. Specificaly, isotropic materials can only be modeled with a Poisson's ratio of 0.25.

2. It is not practical to completely recast classical constitutive models based on stress-strain relationships into a single pairwise force function.

3. Plasticity modeling in bond-based peridynamics allows permanent deformation of materials undergoing volumetric strain, which is inconsistent with real world observations of metals undergoing plastic deformation only as a shear response.

In order to address these limitations in peridynamic modeling of material behavior, a more generalized theory of peridynamics has been formulated called the *state-based* peridynamic theory.

2.2.6 State-based peridynamics and constitutive models

The state-based theory required the development of new mathematical objects called peridynamic states. A state $\underline{\boldsymbol{A}}$ is essentially a transformational operator that acts on a given bond $\boldsymbol{\xi}$ to return a tensor of some order m, which is the called the image of $\boldsymbol{\xi}$ under the state $\underline{\boldsymbol{A}}$ and is denoted $\underline{\boldsymbol{A}}\langle\boldsymbol{\xi}\rangle$ (Silling et al., 2007). The image under a given state may be a tensor of order 1, a vector, in which case the state is a vector state. Similarly, if the image under a given state is a scalar, then it is a scalar state, and so on. Mathematical operations of these peridynamic states have also been defined, the output of which may be a scalar, a vector, a higher order tensor or even another state. The theoretical development of states and related mathematical operations are given in (Silling et al., 2007).

In state-based peridynamics, the material-dependent part of the bond-based theory has been recast. The peridynamic equation of motion consists of a *force vector state* in lieu of a pairwise force function, as shown in Eq. (2.6) (Silling et al., 2007). The force vector state $\underline{\boldsymbol{T}}$ is one of the fundamental parts of the state-based theory that allows each bond's load response to depend on the deformation of its family (Silling et al., 2007). This important difference from the bond-based theory allows materials with any realistic value of Poisson's ratio to be modeled. Moreover, Silling et al., 2007 indicate that $\underline{\boldsymbol{T}}$ is analagous to the stress tensor in the classical theory. Owing to this similarity, classical constitutive models may be translated into a peridynamic constitutive relation.

$$\rho(\boldsymbol{x},t)\ddot{\boldsymbol{u}}(\boldsymbol{x},t)=\int_{\mathcal{H}_x}\left\{\underline{\boldsymbol{T}}\left[\boldsymbol{x},t\right]\left\langle\boldsymbol{x}'-\boldsymbol{x}\right\rangle-\underline{\boldsymbol{T}}\left[\boldsymbol{x}',t\right]\left\langle\boldsymbol{x}-\boldsymbol{x}'\right\rangle\right\}dV_{\boldsymbol{x}'}+\boldsymbol{b}(\boldsymbol{x},t) \quad (2.6)$$

In general, a constitutive relation in the state-based theory defines how the force state $\underline{\boldsymbol{T}}$ depends on something called the *deformation vector state* $\underline{\boldsymbol{Y}}$, as shown below (Silling et al., 2007):

$$\underline{\boldsymbol{T}}=\hat{\underline{\boldsymbol{T}}}\left(\underline{\boldsymbol{Y}},\Lambda\right), \quad (2.7)$$

where $\hat{\underline{\boldsymbol{T}}}$ simply represents a vector state-valued function, meaning its output is a peridynamic vector state, and Λ represents all other variables that $\underline{\boldsymbol{T}}$ depends on other than $\underline{\boldsymbol{Y}}$.

The deformation vector state $\underline{\boldsymbol{Y}}$ is the fundamental kinematic measure in the peridynamic theory (Silling, 2010), analogous to the deformation gradient tensor $\overline{\overline{F}}$ in the classical theory. In traditional continuum mechanics, $\overline{\overline{F}}$ gives a comprehensive description of deformation, including strain and rotation (Brannon, 2008). Similar to the function of $\overline{\overline{F}}$ in the classical framework, $\underline{\boldsymbol{Y}}$ maps an undeformed vector in the reference configuration to its deformed image in the current configuration in a peridynamic framework. It also serves a core function in peridynamic constitutive modeling, as showin in Eq. (2.7). The precise definition is as follows (Silling et al., 2007):

$$\underline{\boldsymbol{Y}}\left[\boldsymbol{x},t\right]\left\langle\boldsymbol{\xi}\right\rangle=\boldsymbol{y}\left(\boldsymbol{x}+\boldsymbol{\xi},t\right)-\boldsymbol{y}\left(\boldsymbol{x},t\right), \quad (2.8)$$

where $\boldsymbol{y}(\boldsymbol{x}, t)$ represents the position of $\boldsymbol{x}$ after the deformation. As indicated, the image of $\boldsymbol{\xi}$ under the deformation is a vector that is analogous to $\boldsymbol{\eta} + \boldsymbol{\xi}$ in the bond-based theory.

2.2.7 Correspondence

The similarity between $\underline{\boldsymbol{Y}}$ and $\overline{\overline{F}}$ becomes useful in an important feature of state-based peridynamics called *correspondence*. The premise begins with a function $\Omega(\cdot) : \mathcal{L}^+ \to \mathbb{R}$ that maps any deformation gradient tensor $\overline{\overline{F}}$ to a corresponding strain energy density in the classical theory. Additionally, suppose that a peridynamic strain energy density function $W(\cdot) : \mathcal{V} \to \mathbb{R}$ exists that maps any deformation vector state $\underline{\boldsymbol{Y}}$ to a corresponding real value of strain energy density such that the following is satisfied for some choice of $\overline{\overline{F}} \in \mathcal{L}^+$ (Silling et al., 2007):

$$\underline{\boldsymbol{Y}}\langle\boldsymbol{\xi}\rangle = \overline{\overline{F}}\boldsymbol{\xi} \quad \forall \boldsymbol{\xi} \in \mathcal{H} \qquad \Longrightarrow \qquad W\left(\underline{\boldsymbol{Y}}\right) = \Omega\left(\overline{\overline{F}}\right). \tag{2.9}$$

Given these conditions, it is said that "the peridynamic constitutive model [based on $\underline{\boldsymbol{Y}}$] *corresponds* to the classical model at $\overline{\overline{F}}$ " (Silling et al., 2007). The corresponding peridynamic model is constructed by first approximating a value of $\overline{\overline{F}}$ from a given $\underline{\boldsymbol{Y}}$ by the reduction of a vector state to a tensor process. Subsequently, the derived $\overline{\overline{F}}$ is used in the classical model Ω to determine $\underline{\boldsymbol{T}}$ based on the implied equality in Eq. (2.9) and the relationship between $\underline{\boldsymbol{T}}$ and W. This idea of correspondence allows for elastic, elastic-plastic and plastic

constitutive models in the classical theory to be appropriately translated into the peridynamic framework for material modeling.

2.2.8 Software implementation

The state-based peridynamic theory has been numerically implemented in a state-of-the-art open source code called *Peridigm*, which is freely distributed out of Sandia National Laboratories and hosted on GitHub. It is the fastest code available running the state-based peridynamic theory of solid mechanics. It is structured in a way that allows the open community of developers to contribute additional functionality, in the form of C++ classes. This simulation software is utilized for this research endeavor.

Chapter 3

Methods

This chapter presents the modeling considerations relevant in the realm of peridynamic simulations and how they may be applied to pulse fracturing. The ultimate objective of this computational study is to determine the fracture behavior resulting from pulse stimulation via a predictive simulation tool. Understanding the generated fracture dimensions and geometry under various subsurface conditions is a critical part of assessing pulse fracturing's viability for the oil and gas industry. In order to facilitate this objective, this study aims to understand how well the computational tool of choice, *Peridigm*, is suited for modeling pulse fracturing. The original work detailed in this thesis can broken down into two major tractable stages, listed as follows:

1. The first stage entails an assessment of *Peridigm*'s capability to capture the general physical phenomenon observed as a result of pulse fracturing, namely, radial fractures initiating at the wellbore wall and propagating into the medium. The modeling choices, required in tailoring this tool to simulate pulse fractures, aid in the subsequent stage of work.

2. The second stage is essentially a benchmarking step for *Peridigm*. It

consists of simulations aimed at matching experimental results from a pulse fracturing study on sandstone core samples.

3.1 Assessing *Peridigm*'s modeling of radial fractures

State-based peridynamic models have been validated to capture dynamic fracturing in brittle materials accurately via numerical implementations such as *Peridigm* (Silling, 2014). It seems logical therefore that *Peridigm* should be able to capture the dynamic radial fractures generated from pulse stimulation. While complexities such as yielding of rock material and heterogeneity may have considerable effects on pulse fractures, the initial assessment of *Peridigm* does away with such confounding factors. In this assessement, the quasi-brittle concrete is chosen as the medium for numerically simulating pulse loading. One compelling reason to choose concrete is that it would be the perfect medium, if ever experimental validation of peridynamic simulations were to be pursued. The availability of near-homogeneous concrete, characterized in even high strain-rate regimes, makes it very suitable for highly controlled and precisely designed experiments.

3.1.1 Model assumptions

In *Peridigm*'s toolkit, the elastic material model is currently the most robust constitutive model available. While other material models exist in the code, they do not support the dependence of material strength and yielding

on mean stress, which is reflective of most real geomaterials. Therefore, the elastic material model is chosen to represent concrete's mechanical behavior, under the assumption that this model adequately describes concrete in dynamic loading. Additionally, concrete is assumed to be homogeneous in order to make the model simpler and hone in on the effects of high-rate loading on fracture behavior. Finally, confining stress is not explicitly modeled.

3.1.2 Material geometry and properties

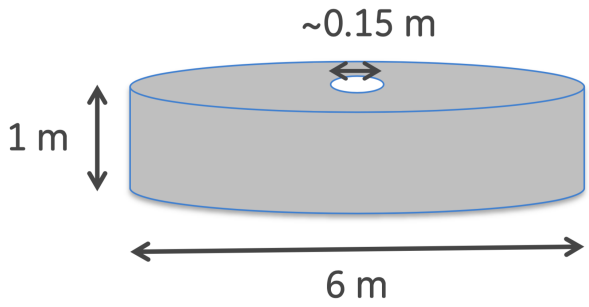

Figure 3.1: Geometry of the model concrete in *Peridigm* simulations.

A simple pulse fracturing case is chosen for these simulations. The model concrete geometry is illustrated in Fig. 3.1. As shown, the sample is a thin cylinder with a hole drilled along its central axis. The diameter and height dimensions are mainly given to convey that the sample has a larger areal extent relative to its height. While the borehole diameter is kept the same in all simulations, slightly varying areal and height dimensions are used. Additionally, the rectangular prism analog of this cylindrical domain is also

simulated for comparison purposes. As far as material properties, typical values for concrete are utilized, as shown in Table 3.1.

Material Properties	
Density, ρ [kg/m^3]	2400
Bulk modulus, K_b [GPa]	23.58
Shear modulus, G [GPa]	16.94

Table 3.1: Concrete material properties.

From the wide range of loading rates in the pulse fracturing regime, the lower end rate of $10\,\mathrm{MPa\,ms^{-1}}$ is opted for, in order to shy away from the explosive fracturing regime as much as possible and minimize the extent of the fully damaged zone around the borehole. For this assessment stage of simulations, a simple linear ramp profile makes sense. The linear profile shown in Fig. 3.2 is used.

3.1.3 Modeling choices

In simulating even this rather simple loading scenario, several modeling considerations arise. These include the choice of mesh type, implementation of boundary conditions and others specific to the peridynamic approach and the *Peridigm* tool. They are individually discussed in some detail.

3.1.3.1 Type of mesh

For numerical simulations, the domain needs to be discretized, for which there is a choice of different element types. The most common choices are tetrahedrons and hexahedrons, which are illustrated in Fig. 3.3, along

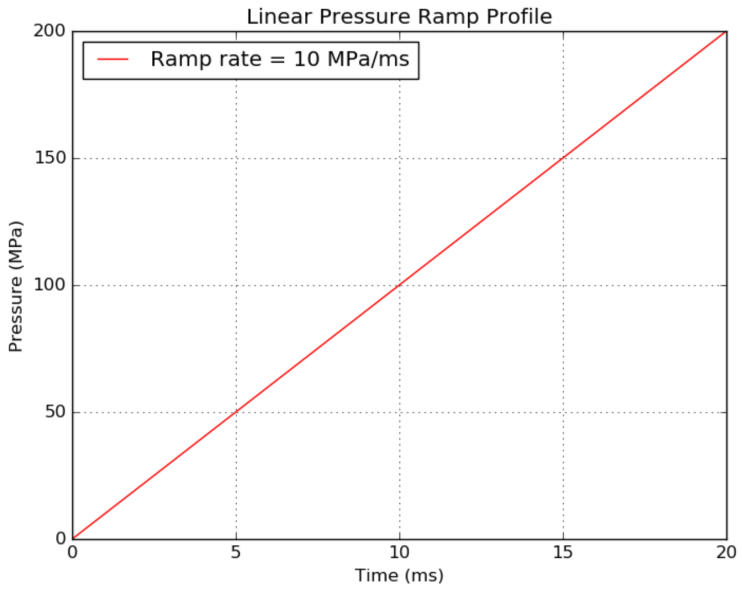

Figure 3.2: Pressure loading profile used in the concrete pulse fracture simulation.

with other less common types. While tetrahedrons are more versatile and allow for adaptive meshing (Frei, 2013), hexahedron elements were chosen in order to reduce the overall number of elements needed to discretize the domain. Because the number of elements is in some sense proportional to the computational time spent in solving a problem, a lower number of elements facilitates faster turnover rate, which allows more simulation runs to explore more parameters. Moreover, generating hexahedron grids for such simple geometries as a cylinder or a rectangular prism can easily be accomplished via short Python scripts.

Among hexahedron meshes, two specific types, Cartesian and

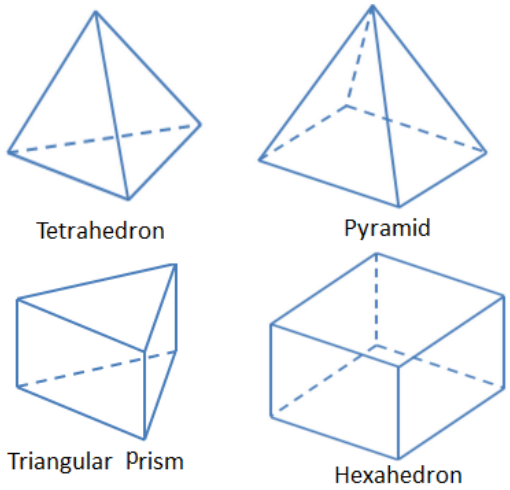

Figure 3.3: 3D element choices in meshing/gridding a simulation domain.

curvilinear, are used in these simulations. These gridding styles are shown in Fig. 3.4. The Cartesian grid is a standard choice, dividing the domain into equally sized cubes. On the other hand, the curvilinear grid was chosen, because many wellbore meshes utilize this scheme. Between these two meshing choices, the better option is decided based on the degree of accuracy and the rate of convergence. Results from these two schemes will be compared in the following chapter.

3.1.3.2 Choice of peridynamic horizon

A key part of these peridynamic simulations is the choice of the *horizon*. This parameter determines the degree of non-locality in the simulation, which ultimately affects the fracture generation. The horizon is a material constant associated with the non-local theory. Unless a whole set of experiments are

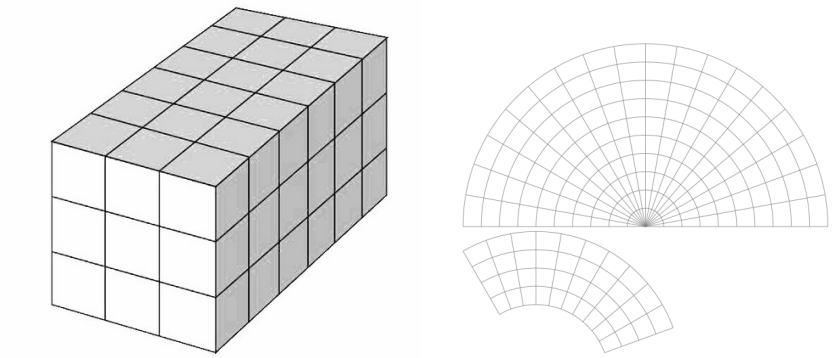

(a) Cartesian grid **(b)** Curvilinear grid

Figure 3.4: Schematics of the two gridding styles used.

conducted to determine each material's microstructure or validated simulations of the material have calibrated parameters, a precise value for the horizon is not readily available. So it is with concrete. A rule of thumb, when such a case is encountered, is to approximate it as 2-3 times the aggregate size of the material at hand. For concrete, the aggregate size is found to be 0.5 in. (PCA, 2016). Hence, the horizon value for concrete may be estimated as 1.5 in. or 0.038 m.

In relation to the horizon, the choice of discretization size also plays an important role. The discretization or mesh size cannot be too small, because this would exponentially increase the the number of elements to be simulated and proportionally increase computational time. The mesh size has an upper bound set by the accuracy of the solution required. Additionally, the mesh size is limited by the amount of resolution required in one horizon's distance from a material point to generate a proper non-local solution. The optimal

discretization size, based on the chosen horizon value, will be discussed in the following chapter.

3.1.3.3 Damage criterion

The value of damage, calculated at each element, is the way fractures are visualized in *Peridigm* simulation results. In order to know when a bond is broken, a damage criterion needs to be defined. For simplicity, the critical stretch damage model is chosen as the requisite criterion, because it has already been implemented in *Peridigm*. The critical stretch value, however, needs to be provided for the material being modeled. Due to the exploratory nature of these simulations, the exact value of this parameter is not critical. Therfore, an arbitrary value of 0.0005 was chosen as the critical stretch at failure.

3.1.3.4 Implementing the boundary conditions

To apply the loading on the surface of the wellbore, traditional finite difference or finite element simulations typically use a pressure boundary condition. Pressure needs to be applied as a traction boundary condition to a distinct surface of the body. This situation presents a challenge in the peridynamic framework. Due to the nature of the formulation, a requirement exists to apply any sort of boundary condition over a volumetric region of the body rather than on a distinct surface. Therefore, an exact surface boundary condition is not possible in peridynamics at the moment, although it is an active area of research.

Typical boundary conditions in peridynamic simulations, as used in *Peridigm* tests and example simulations, are prescribed displacement and body force density. Hence, a couple approaches are attempted to adhere to the peridynamic requirement of a volumetric boundary condition, while applying something akin to pressure on the borehole wall. The first approach takes the route of converting the pressure into an equivalent displacement of elements on which the boundary condition is applied. The transformation is done through an equation that considers stress wave mechanics. It is as follows:

$$\sigma = \rho c v \tag{3.1}$$

$$c = \sqrt{\frac{K_b}{\rho}} \tag{3.2}$$

In Eq. (3.1), σ is the applied stress, which is equivalent to applied pressure p and has dimensions of force per unit area. ρ is the density of the medium, in this case, concrete. v refers to the particle velocity, which is the element velocity in the simulation. c denotes the velocity of the stress waves that propagate through the medium, which can be calculated using Eq. (3.2), where K_b refers to the bulk modulus of the medium.

Because of the symmetry of the circular wellbore, the effective direction of pressure loading is radial. The calculated velocity is therefore radial in direction. It can be broken down into component velocities through coordinate transformations. Subsequently, the component velocities are

converted into displacements by multiplying them by time t. *Peridigm* uses Cartesian coordinates by default. Hence, converting the radial velocity into a prescribed displacement u_i for each element in x and y coordinates results in the following:

$$\begin{aligned} u_x &= vt\frac{x}{\sqrt{x^2+y^2}} \\ u_y &= vt\frac{y}{\sqrt{x^2+y^2}} \end{aligned} \tag{3.3}$$

Using Eqs. (3.1-3.3), a pressure boundary condition is converted to an equivalent prescribed displacement boundary condition. This displacement condition may be applied to a single layer of elements around the borehole, or any thickness into the body of the material. In the concrete simulations, the single layer application as well as applying the boundary condition to a thickness equal to the horizon have been tested to compare the results.

The second approach utilizes the results from a paper by Dr. Bobaru and Dr. Ha at the University of Nebraska-Lincoln, in which convergence is studied when implementing a traction boundary condition in peridynamics (Ha and Bobaru, 2009). The procedure converts the pressure into an equivalent body force density. The body force density b has dimensions of force per unit volume. Therefore, the pressure is initially transformed into a force by multiplying it with the borehole surface area A. Subsequently, the resulting force is divided by volume V, a quantity that denotes the volume of the domain that is represented by the elements on which the boundary condition is applied. To make the body force density as close to a traction as possible, one layer

of elements around the borehole are chosen to apply the boundary condition. The relation between b and p is as follows:

$$b = p\frac{A}{V} \tag{3.4}$$

$$\begin{aligned} b_x &= b\frac{x}{\sqrt{x^2+y^2}} \\ b_y &= b\frac{y}{\sqrt{x^2+y^2}} \end{aligned} \tag{3.5}$$

In Eq. (3.4), the body force density points in the radial direction. Therefore, for Cartesian coordinates, a transformation, as given by Eq. (3.5), needs to applied, similar to the prescribed displacement approach. In these concrete simulations, both approaches are tested in order to determine the best way to model pressure boundary conditions.

3.1.3.5 Workaround for modeling inelasticity

The elastic material model in *Peridigm* is appropriate for certain types of metals and purely brittle materials. For porous material like rock, this model may overestimate the brittle behavior. High-rate loading on a purely elastic material may introduce unrealistic damage zones around the wellbore, which may affect how the wellbore loading is transmitted to the rest of the domain. The ideal solution to address this issue involves implementing a pressure-dependent plasticity model such as the Drucker-Prager constitutive model. In this study, however, a rather crude workaround is utilized whereby the borehole boundary elements were not

allowed to be damaged during loading. The rationale is that, if damage is disallowed in the boundary elements, they remain intact and connected to the main body, enabling continuous transmission of the wellbore pressure boundary condition to the rest of the domain. The effect of this modification will be discussed in following chapter.

3.2 Benchmarking *Peridigm* with experiments

Once *Peridigm*'s capability to model pulse fracturing as well as the procedure to properly model it are understood, the logical next step is to visually match simulation results with some experimental pulse fracturing results from literature. The idea behind this "benchmarking" is to provide some justification that the modeling tool captures the fracture trends evident in experiments. Truly validating this model, however, requires much more experimental data on well-characterized materials than what is currently available in literature. Nevertheless, this benchmarking is a step closer to arriving at a validated predictive tool for determining the viability of pulse fracturing.

The study chosen for this benchmarking step is a set of lab-scale pulse loading experiments done on cylindrical Nugget sandstone core samples by Lawrence-Livermore National Laboratories (Swift et al., 1980). These experiments, while not done following a robust experimental design procedure, are nonetheless great for benchmarking, because the exact pressure pulse profiles used in loading the core samples, as well as

descriptions of the resulting fracture growth are properly logged and published in the study. Some samples have also been photographed to show the fracture growth in cross sections. Therefore, for visual comparison with simulation results, these experiments are indispensable.

3.2.1 Lawrence-Livermore pulse fracture experiments

The core sample loading apparatus used in these experiments is illustrated in Fig. 3.5. The cylindrical core samples are 13 cm in diameter and approximately 15 cm in height (Swift et al., 1980). The sample has a 1.43 cm diameter borehole drilled in the center, which is designated the borehole cavity. Air in the borehole is pressurized by the piston movement, which loads the borehole walls of the core sample and generates fractures, if any. The outside sample faces are coated with an epoxy, which keeps the rock fragments together, should the sample be split from fracturing. Finally, an ambient confining pressure of 0.1 MPa is maintained on the sample by a confining fluid.

The experimentalists load the samples with a number of different pressure profiles. These profile shapes, with their letter designation, are shown in Fig. 3.6. Some profiles exhibit rather large loading rates e.g. profiles *a* and *b*, while others show a long peak pressure maintenance, e.g. profile *f*. Some other profiles suggest slow decay of the pressure pulse e.g. profile *h*. Some core samples are only loaded with one pressure pulse, while others are loaded with multiple pulses of different rates and perhaps different

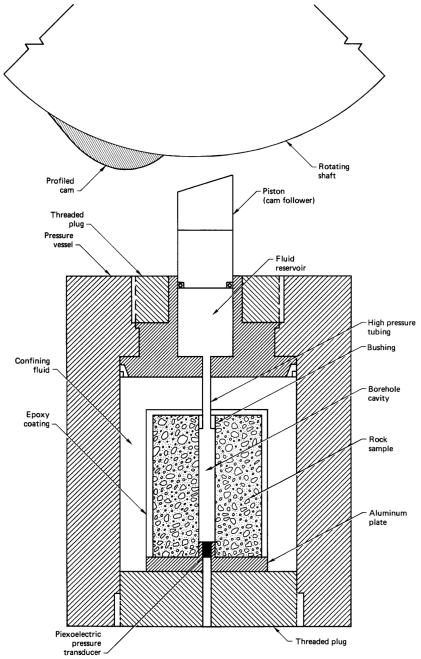

Figure 3.5: Pulse fracturing apparatus in Lawrence-Livermore experiments. (Swift et al., 1980)

profile shapes. The fractures resulting from some of these experimental runs are shown in Fig. 3.7, where the cross sections of core samples reveal the generated fractures.

From these runs, two particular samples are chosen for comparison with *Peridigm* simulations. Sample 6 and sample 11, given as (b) and (e) in Fig. 3.7, indicate two different fracture geometries, generated by two different pressure profiles. The fractures in sample 11 are long and extend to the outer edge of the sample, generated by two pressure pulses of type b loaded in sequence. On the other hand, sample 6 shows short fractures and microcracks, caused by a single pressure pulse of type f.

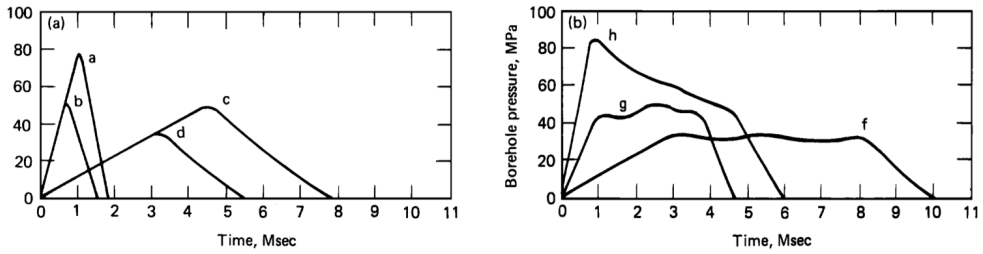

Figure 3.6: Loading profiles used on core samples in Lawrence-Livermore experiments. (Swift et al., 1980)

3.2.2 *Peridigm* simulation approach

3.2.2.1 Material properties

For the same reason as in the concrete modeling, the elastic material model is chosen for sandstone. It is agreed in literature that rock behaves inelastically under certain stress conditions, so this elastic model is admittedly a crude approximation. A mechanical properties study on Nugget sandstone, conducted by Lawrence-Livermore National Laboratories, provides the necessary values required for *Peridigm* simulation input (Schock et al., 1973). The parameters are shown in Table 3.2.

Material Properties	
Density, ρ [kg/m^3]	2560
Bulk modulus, K_b [GPa]	23.5
Shear modulus, G [GPa]	22.1
Young's modulus, E [GPa]	49
Poisson's ratio, ν	0.15
Fracture toughness, K_{Ic} [psi $-$ in$^{1/2}$]	280

Table 3.2: Nugget sandstone material properties. (Schock et al., 1973; Brown et al., 1972)

The choice of the peridynamic horizon δ is yet again a challenge, because it is not available in literature. Moreover, experiments to estimate the value of δ are not in the scope of this study. Therefore, the best option is, similar to the case of concrete, to resort to the rule of thumb: estimate the horizon to be 2-3X the aggregate size. The largest grain size in the classification of sandstone is 2 mm. Hence, based on the heuristic, δ is estimated to be between 4-6 mm.

3.2.2.2 Damage model

For simplicity, the critical stretch damage model is chosen as the failure criterion. A critical stretch value can be calculated based on the protypical microelastic brittle (PMB) material model, developed by Stewart Silling (Silling and Askari, 2005). The equation for critical stretch s_0 in the PMB model is given by Eq. 3.6, where G_0 refers to the critical energy release rate. G_0 is also a material parameter that can be calculated from the fracture toughness K_{Ic}, given in Table 3.2, by means of Eq. 3.7. The upper bound in the range of horizon values, 6 mm, is used for δ. Using the material properties from the table and Eqs. 3.6-3.7, the PMB critical stretch value for Nugget sandstone is determined to be 8.62×10^{-5}.

$$s_0 = \sqrt{\frac{5G_0}{9K_b\delta}} \tag{3.6}$$

$$G_0 = \frac{{K_{Ic}}^2\,(1-\nu^2)}{E} \tag{3.7}$$

3.2.2.3 Model setup

In order to gauge the similarity between the photographed cross sections and the *Peridigm* simulation results, an initial set of coarse mesh simulations are run. These preliminary simulations do not account for the confining pressure nor the epoxy coating around the core samples. Mesh refinement is performed to determine if the simulation output are mesh dependent.

The primary variable in these simulations is the critical stretch parameter s_0 in the damage model. The PMB value for s_0 acts as a lower bound, because it is meant for an elastic and brittle material. Higher values of s_0 are tested to determine if some of the inelasticity and the resulting fracture behavior can be captured. Essentially, the critical stretch takes on the role of the tuning parameter for a match with experimental results.

Meanwhile, as mesh refinement is done, the horizon value is adjusted to the lower end of the range for Nugget sandstone. This adjustment is necessary to maintain reasonable simulation runtimes. Moreover, model additions such as the confining pressure and epoxy coating are incorporated in finer mesh simulations.

Finally, the boundary condition inside the borehole is applied based on the best means to model pressure loading conditions, as determined from the comparison of two approaches in the concrete simulations. The loading profiles for sample 6 and sample 11 are shown in Fig. 3.8.

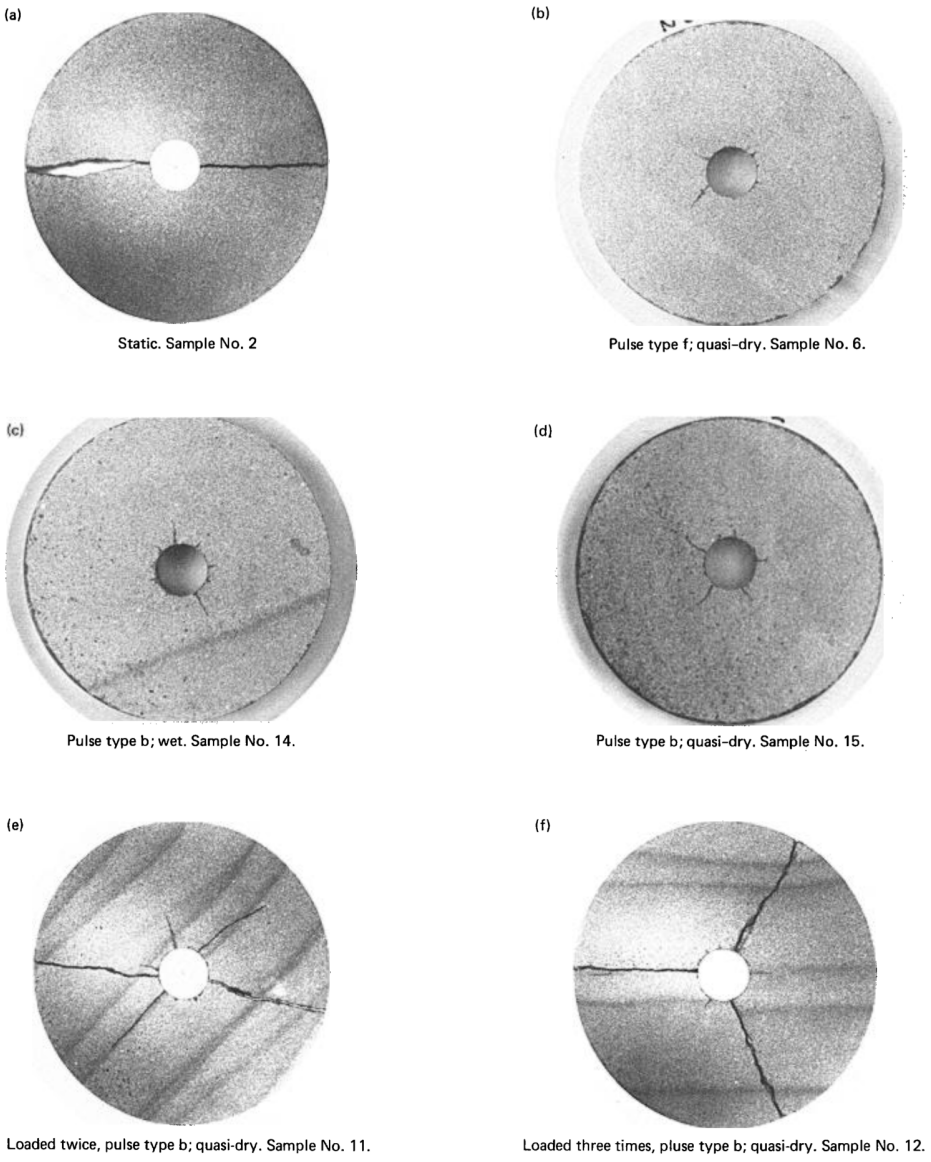

Figure 3.7: Cross sectional photographs of cylindrical core samples, loaded with various pressure pulse profiles. (Swift et al., 1980)

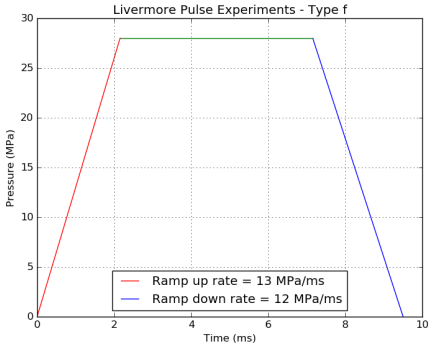

(a) Sample 6

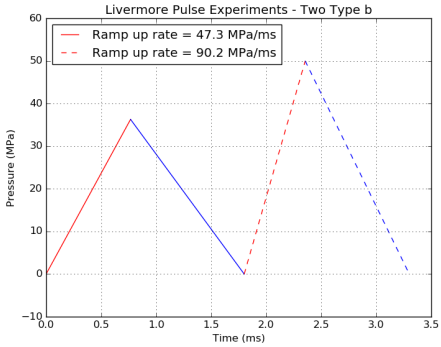

(b) Sample 11

Figure 3.8: Loading profiles for samples 6 & 11 from Lawrence-Livermore experiments.

Chapter 4

Results and Discussion

This chapter explains the simulation results from the assessment and benchmarking stages of work. The concrete simulations from the assessment stage will be presented first. The modeling choices made in this stage and their effects on the simulation results inform how to most appropriately setup a pulse fracturing simulation input. Subsequently, the simulation results from the benchmarking stage, which are compared to the Lawrence-Livermore experiments, will be discussed.

4.1 *Peridigm* assessment results

The initial, purely exploratory simulations test the general effect of borehole loading on a medium at and below the pulse stimulation loading regime. A loading rate of 10 $\mathrm{MPa\,ms^{-1}}$, characteristic of the pulse fracturing regime as indicated in section 2.1.1, is applied in a linear fashion for 20 ms, as depicted in Fig. 3.2, to a cylindrical domain. The domain has the same dimensions as in Fig. 3.1. This loading produces a damage profile as shown in the cross section in Fig. 4.1.

Damage is the quantity referred to in section 2.2.3. While it

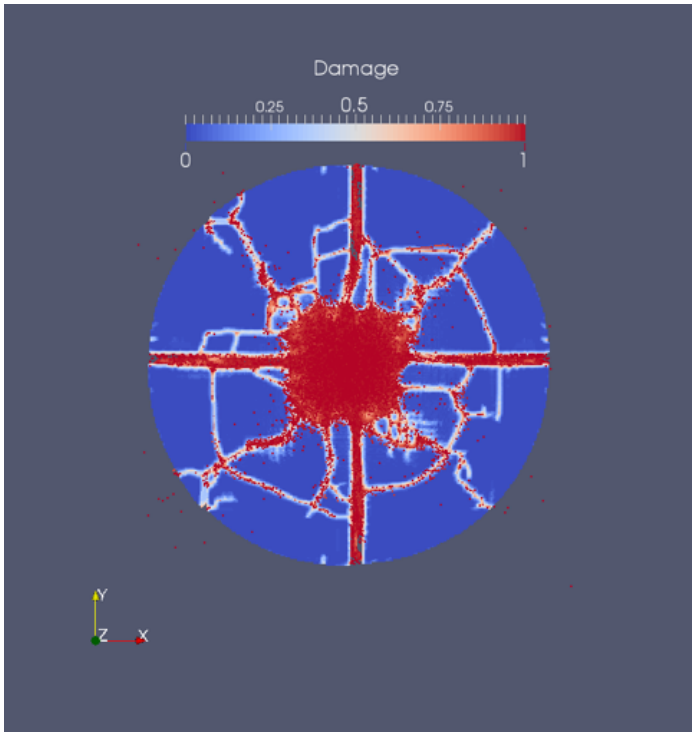

Figure 4.1: Cross sectional damage profile of a cylindrical concrete domain at a 10 MPa ms^{-1} loading rate.

mathematically refers to a fraction of broken bonds, damage contours reveal locations of fractures and other physically destructed zones in a material. Such a damage contour profile can be seen in Fig. 4.1, where the cross section of the cylinder reveals multitudes of fractures that extend from the borehole to the outer edges of the domain. In this scenario, cracks connecting different radially pointing fractures and a large region of 100% damaged elements are also seen. The fully damaged zone, represented by the red contour color, maybe thought of as a rubble zone, consisting of small broken pieces of concrete due to rapid loading. Barring these additional features,

however, the general radial direction of fracture propagation is evident.

It is apparent that the pulse loading caused about 8 major radial fractures. The simulated fracture pattern is visually comparable to the idealized pulse fracturing pattern shown in Fig. 2.1. However, this simulation result has not been tested for mesh dependence, nor have the proper modeling choices been implemented. This particular result is presented purely to indicate that *Peridigm* is able to simulate the radial fracture propagation at intermediate loading rates.

4.1.1 Effect of mesh type

As mentioned in section 3.1.3.1, two hexahedron gridding schemes, curvilinear and Cartesian, are tested in *Peridigm*. The results from the comparison indicate that the Cartesian gridding is the proper choice. The findings leading to this conclusion are detailed below.

4.1.1.1 Curvilinear grid

The grid pattern for a curvilinear meshing scheme is shown in Fig. 3.4b. The elements are smaller close to the center of the discretized domain and progressively increase in size with radial distance. This type of gridding is typically chosen for discretizing a near-wellbore reservoir domain with the wellbore placed at the center. Because both the cylindrical domain depicted in Fig. 3.1 and its rectangular analog match this description, a curvilinear discretization is a reasonable choice.

Based on the results, however, this option seems improper for *Peridigm* simulations. For instance, consider two domains: (1) a cylinder with a 6 m diameter and a 1 m thickness, given in Fig. 3.1, and (2) the same geometry with a larger thickness of 3 m. Both these domains are discretized with a curvilinear grid and loaded with the profile of Fig. 3.2. The results are illustrated in Fig. 4.2.

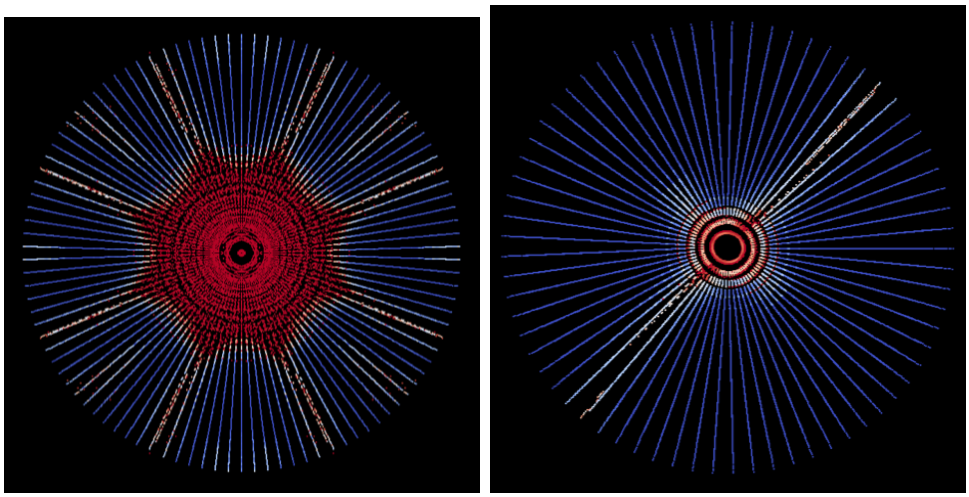

(a) 1 m thick sample **(b)** 3 m thick sample

Figure 4.2: Damage profiles of two samples (curvilinear gridding) loaded with same pulse profile.

In both samples, the borehole loading is applied along the entire length in the axial direction. Also, for reference, both these simulations use the prescribed displacement approach to applying the pressure loading in the borehole. The figure clearly indicates that, while the thinner sample shows an expected symmetric fracture pattern, the thicker one exhibits an oddly asymmetric result. Because there is no heterogeneity introduced into the

model and the loading is radial, the symmetric fracture pattern in Fig. 4.2a is plausible. Increasing the thickness, while it might affect the length of fracture propagation owing to a different amount of dissipated energy, should generally keep the cross sectional fracture pattern the same. This result is a strike against the curvilinear meshing.

4.1.1.2 Cartesian grid

If the same two samples are instead discretized using the Cartesian gridding scheme depicted in Fig. 3.4a, the simulated cases are reconcilable with symmetry expectations. The Cartesian analogs of the two loaded samples are shown in Fig. 4.3.

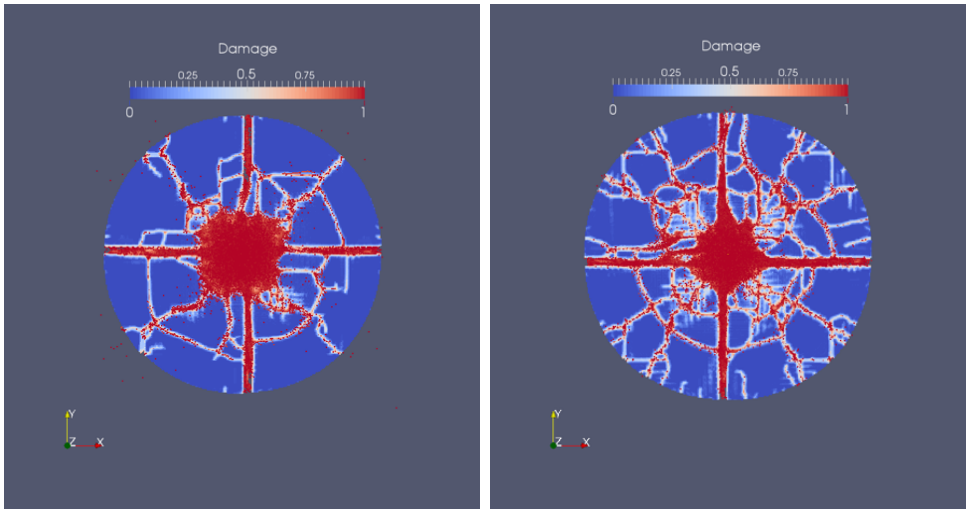

(a) 1 m thick sample **(b)** 3 m thick sample

Figure 4.3: Damage profiles of two samples (Cartesian gridding) loaded with same pulse profile.

The prescribed displacement approach to the pressure boundary

condition is used for these simulations, as in the curvilinear case. Fig. 4.3 shows that the number of radial fractures and even the fracture branching behavior are different in the two different sample thicknesses. These differences are plausible though, considering that the amount of energy dissipated in breaking all the bonds across a fracture would be significantly more for a thicker sample. The important observation to make here is that the radial fracture pattern is symmetric across the quadrants in this cross sectional view. Because neither the loading magnitude nor its direction varies along the axial direction, a change in fracture symmetry is unexpected with merely a change in sample thickness. In this regard, the Cartesian gridding scheme fares better.

To provide additional support for the Cartesian gridding scheme, the rate of convergence is an important factor. Due to the meshfree numerical scheme implemented in *Peridigm* (Silling and Askari, 2005), the discretization type is not inherently relevant. However, because the peridynamic interactions are nonlocal and the computation done at each material point requires information from multiple others within its peridynamic family, the numerical error is amplified when the difference in size between elements in a neighborhood increases (Mathur, 2015). In this regard, uniform meshes tend to provide better rates of convergence in *Peridigm*. Hence, Cartesian gridding is the appropriate choice.

4.1.2 Effect of horizon

Theoretically, the horizon δ is material dependent property, which varies in value based on the scale of the physical phenomenon being modeled. For physics at the nanoscale, δ is "determined by the distance over which physical interactions between atoms and molecules occur" (Silling and Askari, 2005). On the other hand, δ for a macroscale physical phenomenon typically follows a heuristic: $\delta = 3\Delta x$, where Δx refers to the discretization size (Silling and Askari, 2005). This approach aligns with the rule of thumb mentioned in section 3.1.3.2, only if the discretization is chosen to match the characteristic aggregate size of the real material. This match is usually impractical, because of numerical constraints such as computational time and solution accuracy.

For the concrete simulations, the discussion regarding δ will be based on the assumption that the prescribed displacement boundary condition approach is used to load the sample. The initial approach in choosing δ follows Silling's suggestion to use $3\Delta x$. The corresponding simulation results are akin to the ones already shown in Fig. 4.3. There are two glaring issues with this approach:

1. The damage profiles on the cross sections, while showing a generally similar fracture pattern in each quadrant of the xy-plane, do not exhibit perfect symmetry. Given that the borehole loading is radially symmetric and no heterogeneity is introduced into the model, the simulation results

are expected to show perfect symmetry. Even if mesh refinement is deemed necessary to achieve this symmetry, the other issue comes into play.

2. Typically, for any simulation result to be considered valid, the possibility of a mesh-dependent solution must be eliminated. This process of finding a mesh-independent solution is known as a convergence study. If the converged non-local solution is desired, then mesh refinement is performed while holding the horizon fixed at some constant value. This method, however, conflicts with the approach of tying the value of the horizon to the grid size, specifically, by a factor of 3. One could argue also that, by following the $\delta = 3\Delta x$ rule of thumb, every time the mesh is refined, the material being modeled changes.

To address these issues, the value of δ has been set at 0.038 m, through the reasoning detailed in section 3.1.3.2. A mesh-independent solution, while holding δ constant, is sought. In using this approach, a visually similar or unchanged result after mesh refinement is considered a mesh-independent and converged solution. As an example, consider the rectangular prism analog of the concrete model shown in Fig. 3.1. This rectangular sample has a length and width of 4 m, a thickness of 1 m, and the same borehole size as the concrete model. The linear ramp profile, shown in Fig. 3.2, is applied radially over the entire length of the borehole. With δ fixed at 0.038 m, mesh refinement is done, which results in the visually converged solution shown in Fig. 4.4.

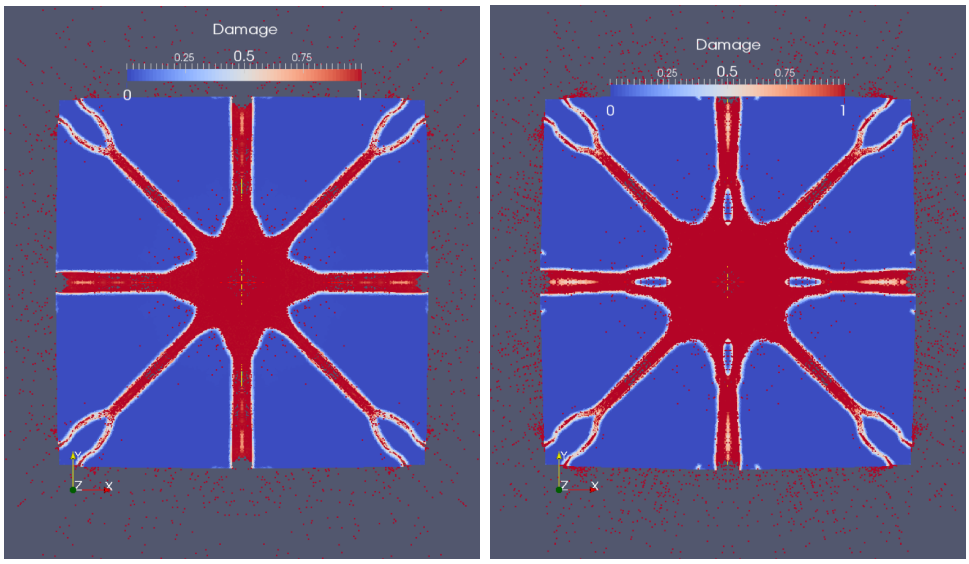

(a) $\Delta x = 0.01$ m **(b)** $\Delta x = 0.008$ m

Figure 4.4: Visual convergence following mesh refinement with a fixed $\delta = 0.038$ m.

From Fig. 4.4, it can be seen that the $\Delta x = 0.01$ m result visually matches the fracture pattern of the finer $\Delta x = 0.008$ m simulation. In this case, the larger discretization can safely be used, as further refinement does not significantly change the picture. Hence, this convergence process, with δ held constant, seems to work, while addressing the issues of symmetry and the horizon being a material constant at a given length scale.

Finally, an important observation regarding the horizon resolution warrants mention in this discussion. In the many trial simulations run using various combinations of horizon and discretization sizes, perfect symmetry is only achieved when $\delta \geq 4\Delta x$. While perfect symmetry makes the simulation results look less realistic, it is not ideal to have unexplained asymmetry arise

in a simulation when perfectly symmetric boundary conditions are applied to a purely homogeneous domain. Therefore, it's important to maintain this level of grid resolution within a horizon's distance from any given element.

4.1.3 Effect of boundary condition implementation

The pressure boundary condition on the surface of the borehole wall can be translated into an equivalent displacement of material points as well as an equivalent body force density. First, the results from the prescribed displacement approach will be discussed. Subsequently, simulation results from the body force density approach will be presented. Incidentally, the body force density condition approximates a true traction boundary condition better than a displacement condition.

4.1.3.1 Prescribed displacement approach

As mentioned in section 3.1.3.4, the prescribed displacement approach converts a pressure condition on a surface into an equivalent displacement of elements via an intermediate radial velocity. In lieu of a surface boundary condition, which is not supported in the peridynamic framework, an equivalent displacement boundary condition can directly be applied as it is associated with a volumetric region. In fact, displacement boundary conditions are among the two most commonly used boundary condition types in peridynamic simulations. Results from applying the equivalent displacement over a single layer of elements and over a δ-thick layer of

elements around the borehole are discussed.

First, the single layer application of the equivalent displacement condition essentially pushes the first layer of elements around the borehole further into the domain, generating strain-induced fractures. For a 6 m x 6 m x 1 m rectangular prism with a central borehole, the linear ramp pressure loading, as in Fig. 3.2, via the displacement of a single layer of elements, generates the damage profile shown in Fig. 4.5.

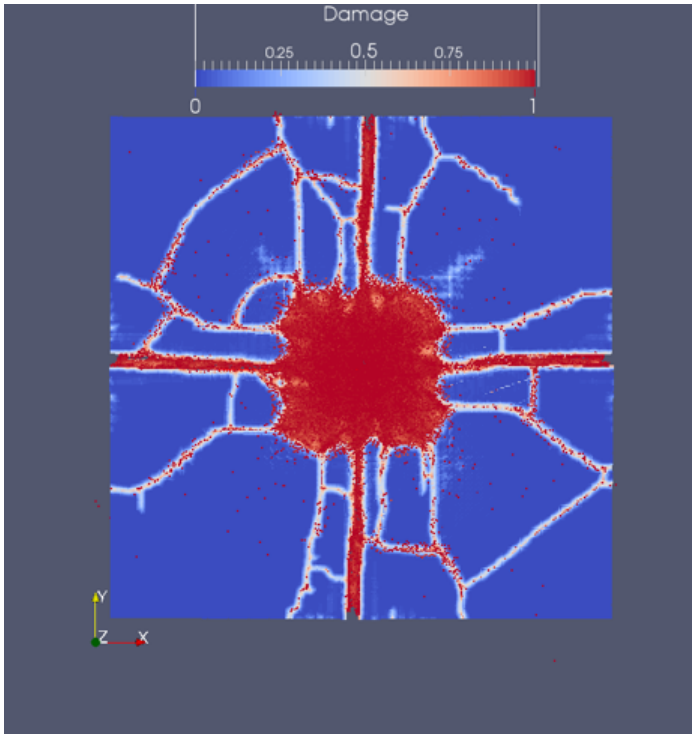

Figure 4.5: A linear ramp pressure pulse applied as a prescribed displacement to a single layer of elements around the borehole.

The damage contours indicate that some fractures propagate radially from the wellbore, while others tangentially connect adjacent radial fractures.

Two issues exist with applying the pressure as an equivalent displacement in this manner:

1. The result exhibits a large region of rubble around the borehole, which represents the explosive fracturing regime more than the pulse fracturing regime. The experimental evidence disagrees with this simulation result, because, at the lower end of the pulse fracturing regime, the rubble zone should in fact be minimal in extent. This outcome suggests that applying an equivalent displacement, at least on a single layer of elements, is not an effective way of modeling a pressurized surface.

2. The single layer of displaced boundary elements actually end up dislodged from the main body before the peak pressure is reached. This behavior cannot be seen in Fig. 4.5, but is apparent when the simulation output is analyzed. These dislodged elements no longer push into the main body, so an active external boundary condition ceases to exist. This phenomenon is starkly different from a pressure boundary condition, which continuously exerts a force on the domain. Because of this behavior, the prescribed displacement approach, at least on a single layer of elements, has a major drawback.

Before dismissing the equivalent displacement approach completely, it may be worth a shot to explore the application to a δ-thick layer of elements. For the same size domain as in the single layer application, the equivalent displacement is now applied to a full horizon thick layer of elements. The

reasoning behind this approach is that, if a thick band of elements are displaced together, due to nonlocal interactions, it is less likely all those elements completely dislodge from the main body. The damage profile for this case is shown in Fig. 4.6.

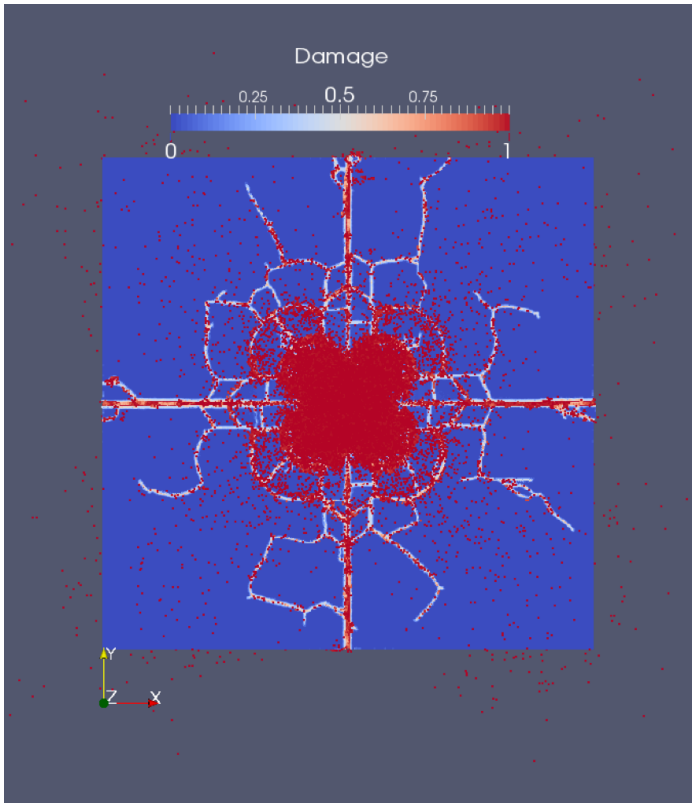

Figure 4.6: A linear ramp pressure pulse applied as a prescribed displacement to a δ-thick layer of elements around the borehole.

It is clear that the larger number of elements being displaced from the center leads to a remarkable difference in the resulting fracture pattern. Compared to the single layer application case, only a fraction of radial fractures extend from the borehole to the outer edges of the domain. On the

other hand, this approach leads to larger number of tangential fractures linking multiple radial fractures. Upon analyzing the simulation output, it is determined that the element dislodging issue is alleviated with this approach. However, the large rubble zone around the borehole still exists. In generating this rubble, a lot of energy is diverted that may actually be used to propagate longer fractures. Hence, the prescribed displacement approach, regardless of the thickness of application, seems unsuitable to capture the effects of a true traction boundary condition.

4.1.3.2 Body force density approach

Similar to the prescribed displacement boundary condition, the body force density boundary condition is also one that is applied over a set of elements that represent some volume of the domain. It is another common type of boundary condition in peridynamic simulations. As described in section 3.1.3.4, this approach takes a traction boundary condition and converts it from a force per unit area to a force density or force per unit volume. In this discussion, the body force density boundary condition is applied to one layer of elements on the borehole wall.

Consider a large cylindrical domain, with a 10 m diameter and a 1 m thickness, that has a borehole drilled in the center with the same dimensions as in Fig. 3.1. After applying the standard linear ramp pressure profile along the length of the borehole, the damage profile that results is shown in Fig. 4.7.

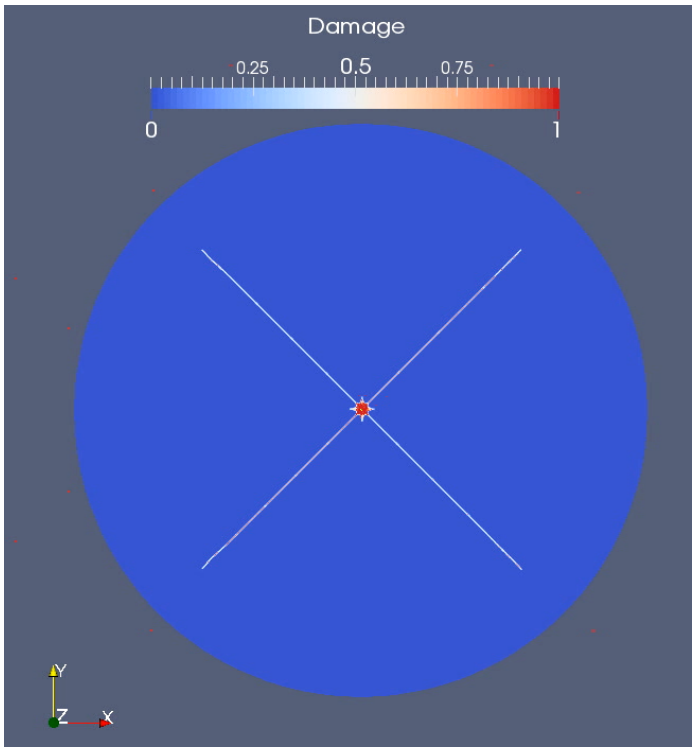

Figure 4.7: A linear ramp pressure pulse applied as a body force density to a single layer of elements around the borehole.

The fracture pattern that results is almost perfectly symmetric, as expected from symmetric loading on a homogeneous domain. There are four long radial fractures and four relatively short radial fractures alternating with the longer ones. The rubble zone is extremely small, preventing additional formation damage around the wellbore. In all visual aspects, this approach seems to produce a comparatively better result than the prescribed displacement approach. Essentially, the application of an equivalent body force density on a single layer of elements around the wellbore closely approximates the intended pressure boundary condition. It also adds support

to this conclusion that researchers at University of Nebraska-Lincoln, as mentioned in section 3.1.3.4, were able to confirm that pressure can be modeled as a body force density in this manner (Ha and Bobaru, 2009).

From the exploratory concrete simulations, some useful and interesting observations surfaced. It became clear that *Peridigm*, when appropriately setup for the problem scenario, is up to the task of simulating pulse fracturing scenarios. The appropriate modeling choices, including mesh type, horizon value and boundary condition type will aid in the simulations that aim to benchmark *Peridigm* against some accessible experimental results published in literature.

4.2 *Peridigm* benchmarking results

Given that the *Peridigm* assessment stage of simulations proved successful, the stage is now set for a comparison of some experimental results with *Peridigm* simulations. The intent is that these simulations may serve as justification that *Peridigm* is a reliable tool to model specific material properties and pressure inputs and to match with real observations. In this case, the match is being done with the Lawrence-Livermore pulse fracturing experiments.

4.2.1 Coarse mesh trials

Initially, the model only considers the sandstone core sample with borehole loading. It neglects the epoxy coating around the samples and the

ambient confining pressure. The higher end of the range in the estimated horizon value, 6 mm, is used for δ, which is held constant. The mesh sizing, Δx, is set at 1 mm. This combination of horizon and mesh size satisfies the requirement, $\delta \geq 4\Delta x$, from section 4.1.2. For these trial simulations, the critical stretch, s_0, is varied between 8.62×10^{-5} and 4×10^{-3}. The lower bound for s_0 comes from the purely elastic value determined from the PMB model in section 3.2.2.2. The chosen upper bound is a high enough value such that no visually significant damage is expected from the loading. Finally, the borehole pressure load is modeled using the body force density approach, as it has been deemed the better alternative.

Using a bisection approach, the range of s_0 values is narrowed to arrive at the target critical stretch value that provides a good match between the simulation results and the cross sectional photographs for samples 6 and 11. Initially, the bisection method is performed with a goal of matching the sample 6 photograph, given as (b) in Fig. 3.7. A s_0 value of 3.8×10^{-4} seems to produce a simulation result that's comparable to the experimental one. The side-by-side comparison is given in Fig. 4.8.

While the simulation result does not capture all of the cross section's features exactly, it resembles the experiment in that the 4 major fractures are of similar length to the longest one from the experiment. The general 90^o spacing between the protruding fractures is also similar to the experimental result. It seems like this s_0 value provides a decent match. However, when a slightly lower value of s_0 is tested, the simulation shows a vastly different

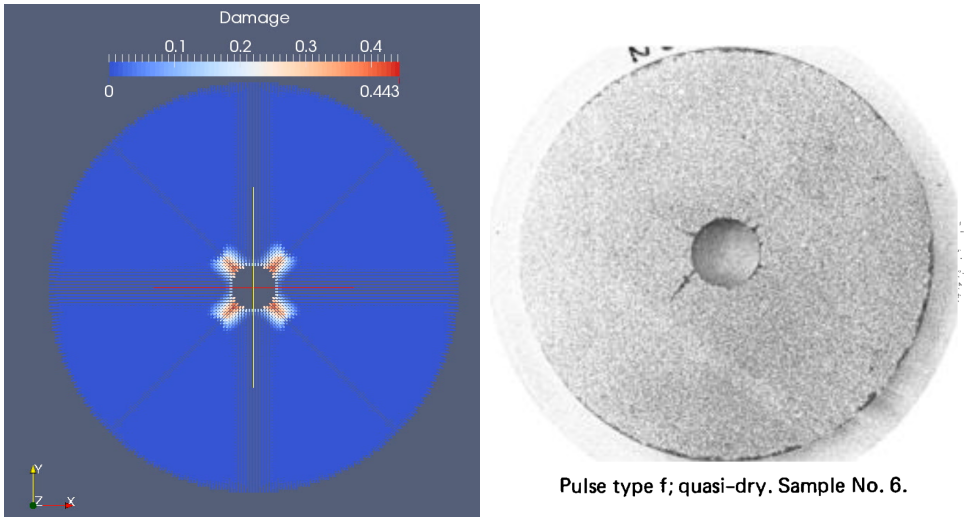

(a) Simulation **(b)** Experiment (Schock et al., 1973)

Figure 4.8: Comparison of simulation and experimental fracture patterns for sample 6 at $s_0 = 3.8 \times 10^{-4}$.

fracture pattern. At an s_0 of 3.77×10^{-4}, the damage profile for sample 6 is illustrated in Fig. 4.9, which shows 4 fractures propagating to the outer edges of the domain.

Based on this marked difference between the results, it is evident that this simulation setup is sensitive to changes in s_0, even in the 6th decimal digit. Alternatively, this phenomenon could be a result of mesh dependency, which translates into a masked effect in the final simulation results. Hence, a finer mesh, with $\Delta x = 0.5$ mm while keeping δ the same, is used to check the consistency of this s_0-sensitivity. The simulation ouput from the finer mesh, with two different values of s_0, are given in Fig. 4.10.

With a finer discretization, even a change in the 5th decimal digit of s_0

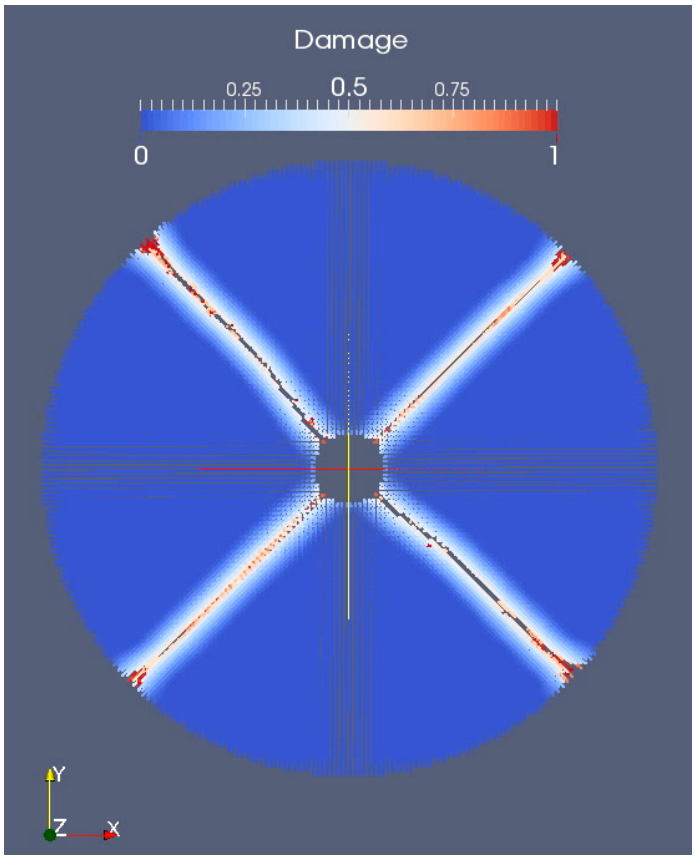

Figure 4.9: Simulation result for sample 6 at $s_0 = 3.77 \times 10^{-4}$.

does not affect the simulation result, let alone in the 6th. Based on Fig. 4.10, the high degree of sensitivity to s_0 is not evident when the mesh is refined. This outcome demonstrates that at least this level of mesh refinement, if not more, is required for the simulation results to be mesh-independent and therefore hold any sort of validity.

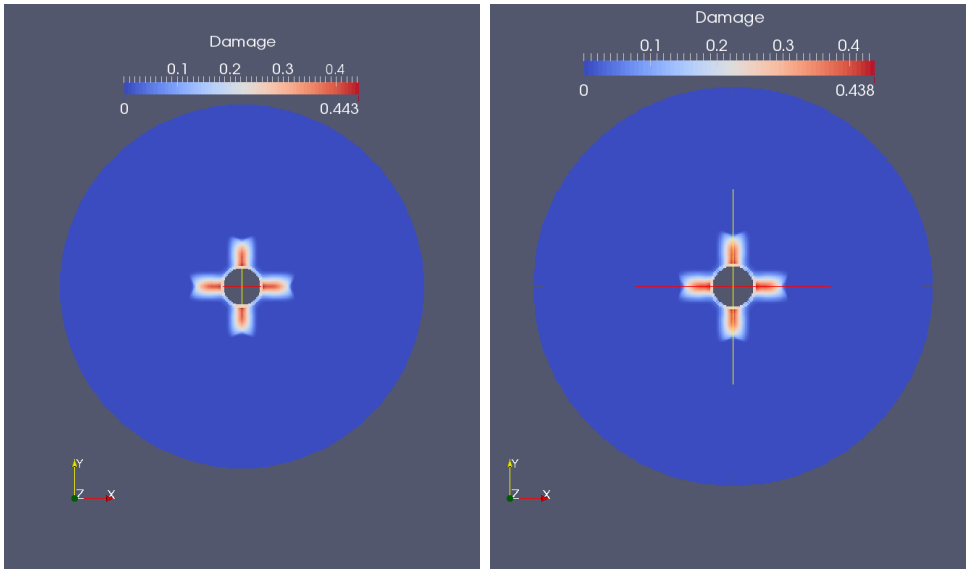

(a) $s_0 = 3.7 \times 10^{-4}$ **(b)** $s_0 = 3.8 \times 10^{-4}$

Figure 4.10: Comparison of finer mesh ($\Delta x = 0.5$ mm) simulation results with different s_0.

4.2.2 Fine mesh simulations

In these simulations, the grid size, Δx, has been reduced to 0.5 mm. Because these simulations are 3D, this halving in the mesh size leads to an almost 8 fold increase in the number of elements. In order to keep the simulation times reasonable, the sample is transformed into almost a 2D circular plane, leaving only a few layers of elements in the height direction. This transformation is assumed to be justified, because the fracture patterns of interest are visualized in the 2D plane already. Therefore, the change in the sample thickness is not expected to have a significant impact. Additionally, for similar computational reasons, the δ value is reduced to 4 mm. This reduces the number of bonds to consider in each time step, while

still remaining in the Nugget sandstone range of estimated horizon values.

Along with a finer discretization, the model is made more sophisticated by the addition of the epoxy and confining fluid. Epoxy is included in the model as a stronger elastic material surrounding the core sample on the sides as well as the top and bottom faces. Similar to the experimental setup, epoxy in the model also seals the top and bottom portions of the borehole, leaving only a fraction of the sample height with an open borehole cavity. The largest thickness of epoxy is on the sides at 0.008 m. The epoxy's material properties utilized in the model setup are given in Table 4.1. The epoxy is meant to hold fragments of the core sample together in case the borehole loading splits it into multiple pieces. Finally, the effect of the confining fluid is modeled as a simple confining pressure of 0.1 MPa, which is implemented via the body force density approach.

Material Properties	
Density, ρ [kg/m^3]	1250
Bulk modulus, K_b [GPa]	7
Shear modulus, G [GPa]	4.2
Critical stretch, s_0	0.008
Horizon, δ [mm]	4

Table 4.1: Epoxy material properties. (Engineering Toolbox Database, 2016)

4.2.2.1 Sample 6

Based on the coarse mesh simulation results, the critical stretch values are limited to $\sim 10^{-4}$. Starting with sample 6, the bisection approach

in this range leads to a small interval of s_0 values, which seem to provide a reasonable match to the experimental fracture patterns. The interval bounds are 1.5×10^{-4} and 2.0×10^{-4}. The simulation results for sample 6 at s_0 values of 1.5×10^{-4}, 1.75×10^{-4}, and 2.0×10^{-4}, along with the experimental cross section, are shown in Fig. 4.11.

From Fig. 4.11, it is evident that these s_0 values produce simulated fractures that are radial in direction and short in extent. While the fracture lengths are not exactly the same as in the experiment, the fracture patterns are visually similar. An observable trend is that, as s_0 is increased, the fractures decrease in length. This trend makes sense, because a larger critical stretch value indicates a greater fracture toughness and hence a higher resistance to fracture. Therefore, the same amount of supplied energy, applied via borehole loading, produces shorter fractures in tougher materials.

When the time evolution of fracture is analyzed from these simulations, it is clear that the majority of fracture propagation occurs during the ramp up in the pressure profile shown in Fig. 3.8a. In this specific pulse, the peak pressure is maintained for a few milliseconds before de-loading. The hold at the peak pressure seems only to elongate the fracture slightly, if at all. The de-loading phase of the pulse does not affect the damage profile.

4.2.2.2 Sample 11

Given some degree of similarity between the simulations and the experiment in the case of sample 6, a good test for this model is to check the

match with the sample 11 experiment using the same s_0 values. The simulations for sample 11 at s_0 values of 1.5×10^{-4}, 1.75×10^{-4}, and 2.0×10^{-4}, as well as the experimental cross section, are shown in Fig. 4.12.

No single s_0 value provides an exact match to the experimental result. However, if the whole interval of values is considered, this set of simulations covers all the fracture lengths observed in the experiment. The longer fractures that extend to the outer boundary, as seen in Fig. 4.12d, are matched by the $s_0 = 1.5 \times 10^{-4}$ case shown in Fig. 4.12a. The simulation result shows the epoxy layer on the boundary in the same color as the rock, but the epoxy does not exhibit damage and keeps the core sample pieces together. Meanwhile, some of the shorter fracture lengths from the experiment are covered by the simulations with higher s_0 values. An exact match with a single s_0 value requires heterogeneity modeling, which is not part of this study. Moreover, heterogeneity of these samples is not quantified by Lawrence-Livermore National Laboratories, which suggests an exact match to these experiments may not be possible.

In the case of sample 11, an analysis of the time evolution of fracture reveals that the two pressure pulses serve different purposes in developing the resulting fracture geometry. Referring to Fig. 3.8b, the first pulse has smaller loading rate and peak pressure values. The simulation results indicate that the first pulse initiates the fracture network and grows the fractures to a certain extent. When the second pulse, with larger loading rate and peak pressure values, hits the sample, the existing network of fractures elongate along the

same direction originated by the first pulse. To illustrate this effect, consider the $s_0 = 1.75 \times 10^{-4}$ case for sample 11. Fig. 3.8b indicates that the ramp up of the second pulse begins at 1.8 ms and peaks at 2.4 ms. The damage profiles at these two times are shown in Fig. 4.13.

From Fig. 4.13a, it can be seen that the first pulse, which completes at 1.8 ms, generates the four main fractures in the geometry. The second pulse, which immediately follows the first and peaks at 2.4 ms, extends the four fractures to greater lengths, as seen in Fig. 4.13b.

The simulations for both samples are reproducible at finer discretizations with no significant changes in the fracture patterns. For instance, at $\Delta x = 0.35$ mm, the damage profiles are almost the same as the ones seen at $\Delta x = 0.5$ mm. Quantitatively, the longest fracture length is not more than 10-12% different at the finer mesh relative to the one at $\Delta x = 0.5$ mm. Therefore, the results at $\Delta x = 0.5$ mm may be considered mesh-independent. Even when the fracture lengths are compared between the simulation and the experiment, the percent error is quite small. As an example, the longest fracture length for sample 6, when compared to the $s_0 = 2.0 \times 10^{-4}$ case, is only 3% shorter in the experiment.

This comparison study shows that *Peridigm*, despite its current limitation in material modeling, can produce a reasonable visual match with experimental pulse fracturing results. One concern from these simulations is the presence of asymmetry. As mentioned in section 4.1.2, asymmetry is not expected when symmetric loading is applied to a homogeneous material. At

this point in the study, the reason for the asymmetry is not fully understood since mesh-sensitivity has already been eliminated. However, a potential factor may be the non-local interaction between the elements of epoxy in the borehole and those of the sandstone material in the borehole wall. Further investigation is required to determine the true source of the asymmetry.

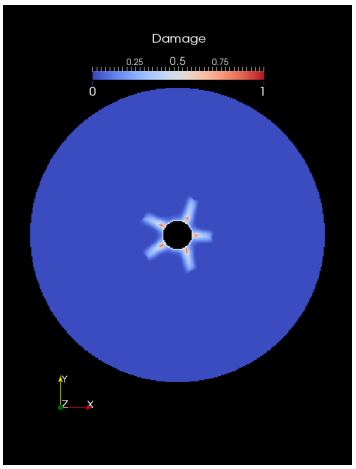

(a) $s_0 = 1.5 \times 10^{-4}$

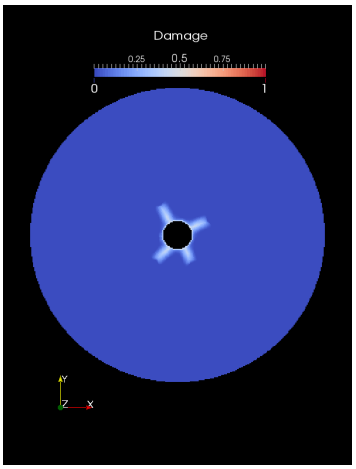

(b) $s_0 = 1.75 \times 10^{-4}$

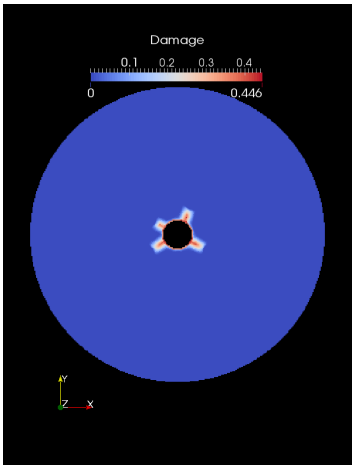

(c) $s_0 = 2.0 \times 10^{-4}$

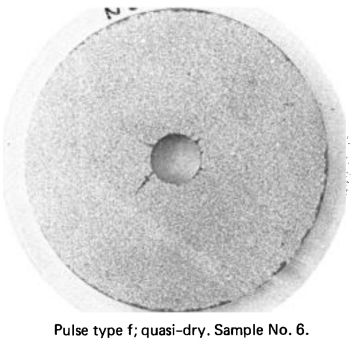

(d) Experiment (Schock et al., 1973)

Figure 4.11: $\Delta x = 0.5$ mm simulation results for sample 6 with 3 calibrated s_0 values compared to the experiment.

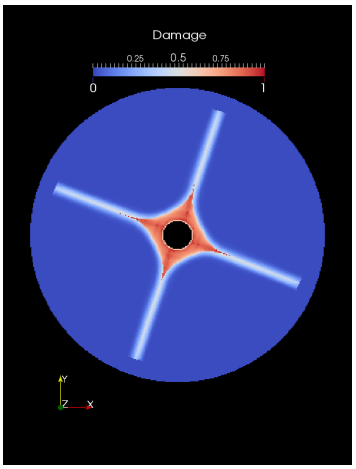

(a) $s_0 = 1.5 \times 10^{-4}$

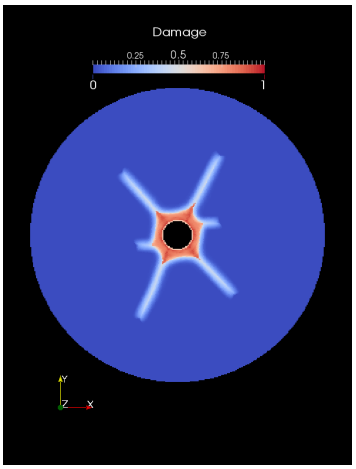

(b) $s_0 = 1.75 \times 10^{-4}$

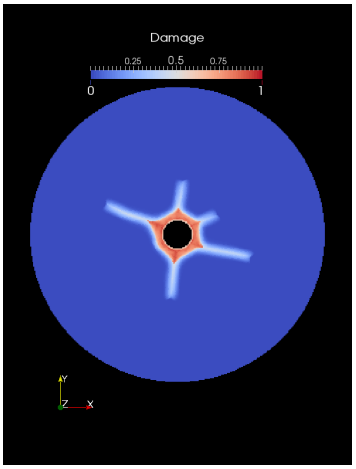

(c) $s_0 = 2.0 \times 10^{-4}$

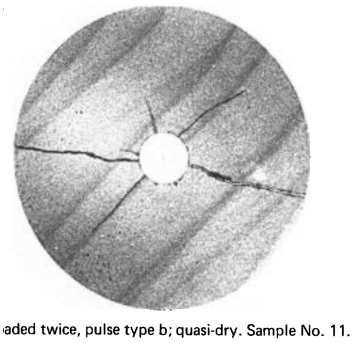

(d) Experiment (Schock et al., 1973)

Figure 4.12: $\Delta x = 0.5$ mm simulation results for sample 11 with 3 calibrated s_0 values compared to the experiment.

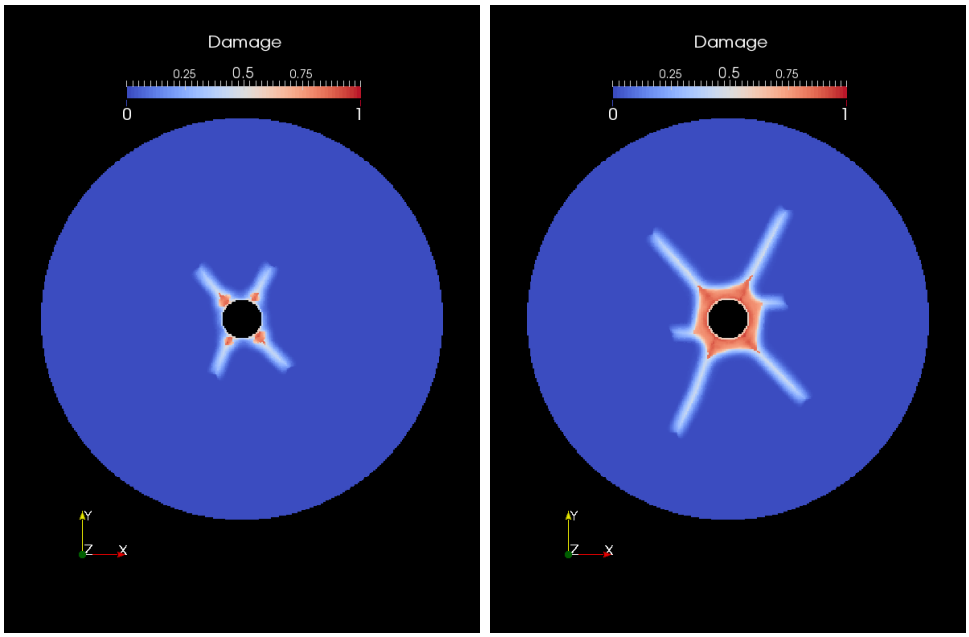

(a) t = 1.8 ms **(b)** t = 2.4 ms

Figure 4.13: Effects of the two pulses in the loading for sample 11.

Chapter 5

Conclusions

This computational study on pulse fracturing primarily focused on assessing the suitability of the simulation tool *Peridigm* to model and simulate pulse fracturing scenarios on geomaterials. The study was broken down into two stages of simulations and analysis:

1. An assessment of *Peridigm*'s general capability to simulate pulse fracture scenarios, which result in a radial fracture pattern, and
2. A benchmarking of *Peridigm* against pulse fracture experiments in literature.

In the assessment stage of simulations, many aspects of modeling in *Peridigm* became clear. Not only did the capability of *Peridigm* to model pulse fracturing scenarios come to light, but some existing limitations and hence opportunities for future work also surfaced. Specifically, the proper ways to discretize domains, to choose a value for the horizon, and to implement boundary conditions, such as pressure, were positive outcomes from this stage of work. These came in handy in preparing input for the benchmarking stage of simulations.

In the benchmarking stage, the value of critical stretch was calibrated to achieve a visual match between the experimental cross sections and the simulation results. A small interval of critical stretch values provided a reasonable match to experiments. It is worthwhile to note that, because the Lawrence-Livermore experiments were not properly designed in terms of replication and randomization, the experimental results may not be statistically significant. Therefore, an imperfect match between the experiments and simulations is expected, especially without explicit modeling of heterogeneity.

5.1 Recommendations for future work

Peridigm currently boasts a robust elastic material model that has been validated in terms of capturing dynamic fracture in brittle materials. This model has been used for representing concrete as well as sandstone in this study. While this elastic model is perfect for purely brittle materials like many metals and ceramics, it is admittedly a crude approximation for modeling quasi-brittle materials, such as concrete, and poroelastic materials, such as rock. It is not representative at all in certain stress regimes, e.g. above the yield stress. For precisely this reason, a pressure-dependent plasticity model is the next step in improving *Peridigm* for modeling geomaterials.

Work is currently underway to implement a plasticity material model based on the Drucker-Prager yield criterion. The Drucker-Prager model has been developed for porous material, including soil and rock (Alejano and

Bobet, 2012). The addition of plasticity should address the issue of a large rubble zone around the borehole under high pulse loading rates. Once this material model is fully incorporated in *Peridigm*, the benchmarking trial simulations may be repeated for a comparison with the results based on the purely elastic model.

Meanwhile, *Peridigm* may also benefit from adding an option for an absorbing boundary layer. For finite domains, there is no need for such an option. In *Peridigm* simulations, stress wave reflections at the boundary may cause crack growth originating from the outer boundary. This computational behavior is tolerable because this is a physical phenomenon that is expected in finitely-sized real media. However, when psuedo-infinite domains such as subsurface rock need to be modeled, this absorbing boundary layer is necessary, because a finite computational domain in *Peridigm* needs to mimic a rather large subsurface region of rock. An absorbing boundary layer impinges "waves at the computational boundaries so they do not reflect back into the simulation" (Wildman and Gazonas, 2013). In this manner, a psuedo-infinite or even an infinite domain may be modeled in *Peridigm*.

With the addition of plasticity and an absorbing boundary layer, *Peridigm* will be equipped to handle large domains of subsurface rock. Once further benchmarking is done using plasticity, a pulse fracture profiling study is an appropriate next step. A quantitative study on fracture behavior, e.g. length, orientation, and branching, under various subsurface conditions, including variations in far-field stress magnitudes and stress anisotropies, will

provide a guide on when and where pulse fracturing is an appropriate choice for stimulation. Moreover, a pressure profile study that tests the effects of single and multiple pressure pulses and their respective loading rates will aid in the design of pulse stimulation treatments. These recommendations, for improving *Peridigm* and designing simulation cases, should motivate further research in this computational study.

Bibliography

Alejano, L. R. and Bobet, A. (2012). Drucker–prager criterion. In *The ISRM Suggested Methods for Rock Characterization, Testing and Monitoring: 2007-2014*, pages 247–252. Springer.

Brannon, R. (2008). What is deformation? `http://www.mech.utah.edu/~brannon/public/Deformation.pdf`.

British Petroleum Energy Report (2016). Bp energy outlook - 2016 edition. `https://www.bp.com/content/dam/bp/pdf/energy-economics/energy-outlook-2016/bp-energy-outlook-2016.pdf`.

Brown, W. S., Swanson, S. R., and Mason, W. E. (1972). Fracture mechanics applications to rock. Technical report, DTIC Document.

Cuderman, J., Chu, T., Jung, J., and Jacobson, R. (1986a). High energy gas fracture experiments in liquid-filled boreholes: potential geothermal application. Technical report, Sandia National Labs., Albuquerque, NM (USA).

Cuderman, J. et al. (1986b). Tailored-pulse fracturing in cased and perforated boreholes. In *SPE Unconventional Gas Technology Symposium*. Society of Petroleum Engineers.

Cuderman, J., Northrop, D., et al. (1986c). A propellant-based technology for multiple-fracturing wellbores to enhance gas recovery: application and results in devonian shale. *SPE Production Engineering*, 1(02):97–103.

Druet, P. A. and O'Connor, S. J. (1991). High-energy gas fracturing succeeds in central lake erie. *Oil & Gas Journal*, 89(51).

Engineering Toolbox Database (2016). Engineering materials. `http://www.engineeringtoolbox.com/engineering-materials-properties-d_1225.html`. Accessed: 2016-08-09.

Frei, W. (2013). Meshing your geometry: When to use the various element types. COMSOL Blog, `https://www.comsol.com/blogs/meshing-your-geometry-various-element-types/`.

Gale, J. F., Reed, R. M., and Holder, J. (2007). Natural fractures in the barnett shale and their importance for hydraulic fracture treatments. *AAPG bulletin*, 91(4):603–622.

Ha, Y. and Bobaru, F. (2009). Traction boundary conditions in peridynamics: a convergence study. Technical report, Technical report Department of Engineering Mechanics, University of Nebraska–Lincoln, Lincoln, Nebraska.

Jaimes Plata, M., Castillo, R. D., Mendoza, S. A., et al. (2012). High energy gas fracturing: A technique of hydraulic prefracturing to reduce the pressure losses by friction in the near wellbore-a colombian field application. In *SPE*

Latin America and Caribbean Petroleum Engineering Conference. Society of Petroleum Engineers.

Li, D., Zhao, G., Yang, W., et al. (1995). High energy gas fracturing (hegf): Mechanism and practice. In *International Meeting on Petroleum Engineering*. Society of Petroleum Engineers.

Littlewood, D. J. (2015). Roadmap for peridynamic software implementation. Technical report, Sandia National Laboratories.

Mathur, R. (2015). What is the main difference between a uniform mesh and non-uniform mesh? `https://www.quora.com/What-is-the-main-difference-between-a-uniform-mesh-and-non-uniform-mesh`. Accessed: 2016-11-23.

PCA (2016). Aggregates. Portland Cement Association, `http://www.cement.org/cement-concrete-basics/concrete-materials/aggregates`.

PetroWiki Database (2015). Formation damage. `http://petrowiki.org/Formation_damage`. Accessed: 2016-11-21.

Safari, M. R. (2013). Pulsed fracturing in shale reservoirs: geomechanical aspects, ductile-brittle transition and field implications. Unconventional Resources Technology Conference (URTEC).

Safari, R., Huang, J., Mutlu, U., Glanville, J., et al. (2014). 3d analysis and engineering design of pulsed fracturing in shale gas reservoirs. In *48th*

US Rock Mechanics/Geomechanics Symposium. American Rock Mechanics Association.

Schlumberger Brochure (2008). Characterization of fractured reservoirs: Reliable, predictive models to optimize carbonate reservoir performance. Brochure available at `https://www.slb.com/carbonates`.

Schock, R., Abey, A., Bonner, B., Duba, A., and Heard, H. (1973). Mechanical properties of nugget sandstone. Technical report, Lawrence-Livermore National Laboratories.

Silling, S. A. (2000). Reformulation of elasticity theory for discontinuities and long-range forces. *Journal of the Mechanics and Physics of Solids*, 48(1):175–209.

Silling, S. A. (2010). Linearized theory of peridynamic states. *Journal of Elasticity*, 99(1):85–111.

Silling, S. A. (2014). Multiscale modeling of fracture with peridynamics. Technical Powerpoint Presentation.

Silling, S. A. and Askari, E. (2005). A meshfree method based on the peridynamic model of solid mechanics. *Computers & structures*, 83(17):1526–1535.

Silling, S. A., Epton, M., Weckner, O., Xu, J., and Askari, E. (2007). Peridynamic states and constitutive modeling. *Journal of Elasticity*, 88(2):151–184.

Stoller, H. et al. (1985). A perspective on tailored pulse loading: A new approach to oil and gas well stimulation. In *SPE/DOE Low Permeability Gas Reservoirs Symposium*. Society of Petroleum Engineers.

Swift, R., Kusubov, A., et al. (1980). Technique for studying multiple fractures produced at intermediate loading rates. In *The 21st US Symposium on Rock Mechanics (USRMS)*. American Rock Mechanics Association.

Warpinski, N. R., Schmidt, R., Walling, H., Cooper, P., and Finley, S. (1978). High energy gas frac. Technical report, Sandia Labs., Albuquerque, NM (USA).

Wildman, R. A. and Gazonas, G. A. (2013). A perfectly matched layer for peridynamics in two dimensions. *Journal of Mechanics of Materials and Structures*, 7(8):765–781.

Yang, W., Zhou, C., Qin, F., Li, D., et al. (1992). High-energy gas fracturing (hegf) technology: research and application. In *European Petroleum Conference*. Society of Petroleum Engineers.